JOURNAL OF PETROLOGY | VOLUME 51 | NUMBER 11 | PAGES 2303–2325 | 2010 | doi:10.1093/petrology/egq058

Petrology of Nepheline Syenite Pegmatites in the Oslo Rift, Norway: Zirconium Silicate Mineral Assemblages as Indicators of Alkalinity and Volatile Fugacity in Mildly Agpaitic Magma

T. ANDERSEN[1]*, M. ERAMBERT[1], A. O. LARSEN[2] AND R. S. SELBEKK[3]

[1]DEPARTMENT OF GEOSCIENCES, UNIVERSITY OF OSLO, PO BOX 1047 BLINDERN, N-0316 OSLO, NORWAY

[2]STATOIL ASA, HYDROVEIEN 67, N-3908 PORSGRUNN, NORWAY

[3]NATURAL HISTORY MUSEUM, UNIVERSITY OF OSLO, SARS GATE 1, N-0562 OSLO, NORWAY

RECEIVED APRIL 7, 2010; ACCEPTED SEPTEMBER 7, 2010

Agpaitic nepheline syenites contain complex zirconium silicate minerals as primary magmatic phases; agpaitic liquidus mineral assemblages are controlled by compositional parameters such as alkalinity and concentrations of water and halogens in the magma. The Larvik Plutonic Complex in the late Palaeozoic Oslo Rift, Norway consists of hypersolvus monzonite (larvikite) and different varieties of nepheline syenite. The nepheline syenite members have miaskitic mineralogy (i.e. zircon stable), except for a suite of late, mildly agpaitic pegmatites, which contain zirconium silicate minerals of the wöhlerite, rosenbuschite and eudialyte groups, in some cases together with zircon. These minerals form part of the liquidus mineral assemblage of the nepheline syenite magma together with fluorite and the rock-forming minerals alkali feldspar, aegirine(–augite), alkali amphibole, biotite, nepheline and sodalite. Low-variance mineral assemblages with two or three zirconium silicate minerals, fluorite and the major rock-forming minerals can be modelled in terms of phase equilibria in a multi-component system involving the sodium disilicate component of the melt and the volatile components water, fluorine and chlorine. A semiquantitative isothermal and isobaric petrogenetic grid in log activity space constructed from the observed mineral assemblages and the compositions of the coexisting minerals indicate that there are at least three trends of evolution leading from a miaskitic to an agpaitic crystallization regime in peralkaline nepheline syenites: (1) the increasing alkalis trend, typically leading to eudialyte-dominated liquidus assemblages (and possibly further to hyperagpaitic residual liquids); (2) the increasing water trend, leading to catapleiite crystallization; (3) the increasing fluorine trend, giving transitionally agpaitic liquidus assemblages with wöhlerite, låvenite and hiortdahlite, with or without zircon, but eventually with magmatic fluorite; this type of evolution is applicable to weakly agpaitic systems such as the Oslo Rift pegmatites. The evolution of such magmas will most probably terminate at liquidus boundaries also involving eudialyte and/or rosenbuschite, and they are unlikely to evolve to more strongly agpaitic compositions.

KEY WORDS: *agpaitic rocks; Oslo Rift; nepheline syenite; zirconium silicate minerals*

INTRODUCTION

Zircon is an abundant accessory mineral, and in most igneous rocks it is the main host mineral for zirconium. Factors that control the crystallization of zircon from a silicate melt include the concentration of zirconium, the major element composition and volatile content of the magma, as well as temperature (e.g. Watson & Harrison, 1983; Baker *et al.*, 2002). However, in some highly evolved

*Corresponding author. E-mail: tom.andersen@geo.uio.no

Table 1: Mineral formulas for Zr-silicates and other important minerals from nepheline syenite pegmatites in the Oslo Rift

Eudialyte-group	
Eudialyte	$Na_{15}Ca_6(Fe^{2+},Mn^{2+})_3Zr_3(Si_{25}O_{73})(O,OH,H_2O)_3(OH,Cl)_2$
Ferrokentbrooksite	$Na_{15}Ca_6(Fe,Mn)_3Zr_3NbSi_{25}O_{73}(O,OH,H_2O)_3Cl_2$
Zirsilite-(Ce)	$(Na_{11-12})(Ce,Na)_3Ca_6Mn_3Zr_3Nb(Si_3O_9)_2(Si_9O_{27})_2(SiO)(OH)_3CO_3{\cdot}H_2O$
Wöhlerite group	
Wöhlerite	$Na_2Ca_4ZrNb(Si_2O_7)_2O_3F$
Hiortdahlite	$Na_2Ca_4Zr(Nb,Ti)(Si_2O_7)_2(F,O)_4$
Låvenite	$Na_2(Na,Ca)_2(Fe^{2+},Mn,Ti)_2(Nb,Zr)_2(Si_2O_7)_2(O,F)_4$
Rosenbuschite group[1]	
Rosenbuschite	$(Ca,Na)_3(Zr,Ti)Si_2O_7FO$
Hainite	$Na_2Ca_5(Ti,Zr,Mn,\square)(Si_2O_7)_2F_2(OH)_2$
Kochite	$(Na,Ca)_3Ca_2(Mn,Ca)ZrTi(Si_2O_7)_2(F,O)_4$
Grenmarite	$(Zr,Mn)_2(Zr,Ti)(Mn,Na)(Na,Ca)_4(Si_2O_7)_2(O,F)_4$
Rinkite group	
Mosandrite[2]	$Ti(\square,Ca,Na)_3Ca_4(Si_2O_7)_2[H_2O,OH,F]_4 \cdot \sim 1H_2O$
Rinkite ('Johnstrupite'[3])	$Ti(Na,Ca)_3(Ca,Ce)_4(Si_2O_7)OF_3$
Catapleiite	$Na_2ZrSi_3O_9 \cdot 2(H_2O)$
Tritomite-Ce	$(Ce,Ca,La,)_5(Si,B)_3(O,OH)_{12}(OH)$
Pyrochlore	$(Na,Ca)_2Nb_2(O,OH,F)_7$

Formulas after Strunz & Nickel (2001) with additional data from the www.mindat.org database (http://www.mindat.org/strunz.php).
□: Vacancy.
[1]Christiansen *et al*. (2003). [2]Bellezza *et al*. (2009). [3]Brøgger (1890).

felsic rocks, zircon is absent despite a high concentration of zirconium. In such rocks, Zr is hosted by complex zirconium silicate minerals, some of which are listed in Table 1 (e.g. Sørensen, 1974, 2006; Khomyakov, 1995; Salvi & Williams-Jones, 1995; Schilling *et al*., 2009). Based on studies of nepheline syenite intrusions in the Gardar Rift in Greenland, Ussing (1912) introduced the term agpaite for nepheline syenite with $(Na + K)/Al \geq 1{\cdot}2$. In current petrographic terminology, agpaitic rocks are peralkaline nepheline syenites with complex Na–Ca–Ti–Zr-silicate minerals (Le Maitre, 2003). In contrast, less alkaline nepheline syenites in which zircon, titanite and ilmenite are characteristic minerals are called miaskitic, from a rock name originally coined for a non-peralkaline nepheline syenite (Le Maitre, 2003). Agpaitic nepheline syenites are major constituents of large, highly alkaline intrusive complexes such as the Ilímaussaq intrusion in southern Greenland and the Khibina and Lovozero intrusions in the Kola Peninsula, but they also occur as minor intrusive members in dominantly miaskitic alkaline rock complexes (e.g. Motzfeldt and Gardiner complexes, Greenland; McGerrigle and Mont Saint-Hilaire, Canada; Oslo Rift, Norway; Sørensen, 1997, and references therein), and agpaitic mineral assemblages have formed by late- to post-magmatic, fluid-induced processes in miaskitic nepheline syenite in Tamazeght, Morocco (Schilling *et al*., 2009, and references therein).

The factors controlling the transition from a miaskitic (i.e. zircon present) to an agpaitic liquidus mineralogy with complex zirconium silicate minerals in a peralkaline nepheline syenite magma is an important problem in the petrology of alkaline rocks. An elevated sodium concentration in the magma is clearly needed to stabilize minerals such as sodium catapleiite ($Na_2ZrSi_3O_9{\cdot}2H_2O$) in nepheline syenite or elpidite ($Na_2ZrSi_6O_{15}{\cdot}3H_2O$) in alkali granite, and strong enrichment of alkali elements and other incompatible components by extensive fractional crystallization of an alkaline parent magma is generally thought to be necessary for the formation of agpaitic magmas (e.g. Larsen & Sørensen, 1987). However, the zirconium silicate minerals listed in Table 1 also contain essential water, fluorine or chlorine, and the activities of volatile species in the magma will influence the mineralogy of zirconium-bearing phases in such rocks (e.g. Kogarko, 1974; Sørensen, 1997). The effect of halogens to stabilize complex Na–Ca–Zr silicates was, in fact, pointed out already by Brøgger (1890) in his classical study of the minerals of nepheline syenite pegmatites in the Oslo Rift, Norway.

One convenient way to evaluate the relative effects of alkalinity and volatile activities for the transition from miaskitic to agpaitic conditions in nepheline syenite magmas is to examine zirconium silicate mineral assemblages in groups of cogenetic rocks with both miaskitic and agpaitic members. The nepheline syenite pegmatites in the Oslo Rift (Larsen, 2010) provide one such example. These pegmatites range from zircon-bearing to zircon-free types, and have provided the type specimens for catapleiite, wöhlerite, hiortdahlite, låvenite and other minerals. Based on the mineral assemblages of these pegmatites, Semenov (in Sørensen, 1974) defined the Langesundsfjord type as a separate class of nepheline syenite, intermediate between the main miaskitic and truly agpaitic types, and Khomyakov (1995) assigned them to the low agpaitic rocks. Despite nearly two centuries of active mineralogical research (Larsen, 2010, and references therein), no studies have been made on the petrology of these pegmatites since that by Brøgger (1890), and their coexisting zirconium silicate mineral assemblages have not been properly characterized.

Here we report the results of a systematic study of the zirconium silicate mineral assemblages and mineral compositions in selected nepheline syenite pegmatites from the Larvik Plutonic Complex in the Oslo Rift. These data provide the basis for a chemographic analysis in

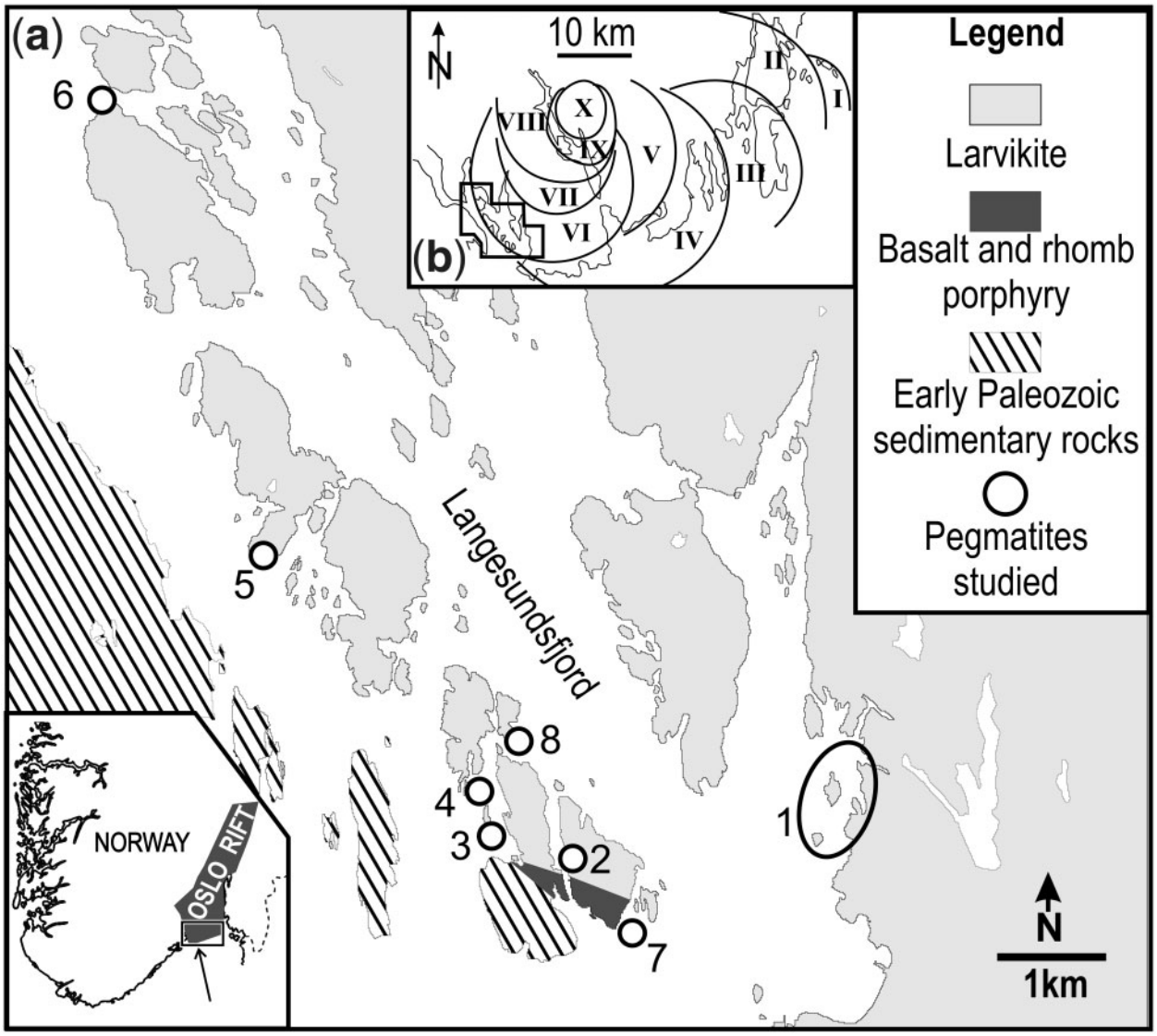

Fig. 1. (a) Simplified geological map of the Langesundsfjord archipelago and surrounding area, SW Oslo Rift, Norway. Localities: 1, Barkevik area (including Barkevik, Barkevikskjær, Skutesundskjær, Kjeøya); 2, Stokksund; 3, Langodden; 4, Arøyskjærene; 5, Risøya; 6, Trompetholmen; 7, Låven; 8, Vesle Arøya. (b) Simplified map showing the 10 successive ring segments making up the Larvik Plutonic Complex, after Petersen (1978). Location of the map area in (a) is indicated.

multi-component space, which is used to derive an empirical, semiquantitative petrogenetic grid relating the zirconium silicate liquidus mineralogy to alkalinity and volatile activities. This, in turn, provides constraints for the relative importance of the parameters controlling the transition from a miaskitic to an agpaitic crystallization regime in peralkaline nepheline syenite magma.

GEOLOGICAL SETTING

The Oslo Rift in southeastern Norway is part of a system of late Carboniferous to Permian continental rifts in northern Europe (Neumann *et al.*, 2004). Rift-related igneous rocks range in composition from alkaline basalt to granite and nepheline syenite, with a large proportion of intermediate, monzonitic intrusive rocks (larvikite) and compositionally equivalent latitic lavas known as rhomb porphyries (Neumann *et al.*, 2004, and references therein). The Larvik Plutonic Complex (Fig. 1b) is a large, composite intrusion making up the southernmost onshore part of the Oslo Rift (Larsen *et al.*, 2008; Dahlgren, 2010). The complex is built up of 10 arc-shaped or circular intrusions of hypersolvus monzonite (larvikite) and nepheline syenite (Fig. 1b; Petersen, 1978). U–Pb dating of magmatic zircon suggests a relatively short period of emplacement and crystallization (299–292 Ma, Dahlgren, 2010), overlapping in

time with the main rifting episode and widespread rhomb porphyry volcanism (Larsen *et al.*, 2008). Trace element distribution patterns and radiogenic isotopic signatures of larvikite and rhomb porphyry point towards an origin from the lithospheric mantle (Neumann *et al.*, 2004, and references therein). The rocks of the Larvik Plutonic Complex range from mildly quartz normative in the early, eastern ring intrusions, to strongly nepheline normative in the younger intrusions in the west and north (Petersen, 1978). This range in composition is explicable by polybaric fractionation of a mildly alkaline, mafic parent magma in deep- to middle-crustal magma chambers, combined with a density filtering mechanism (Neumann, 1980).

Syenite and nepheline syenite pegmatites are relatively common in the Larvik Plutonic Complex (Dahlgren, 2010), and can be grouped in three main suites.

(1) Miaskitic pegmatites with zircon, titanite, pyrochlore and zirconolite ('polymignite'), known as the eastern type, as they are mainly found in the eastern part of the complex.
(2) Mildly agpaitic nepheline syenite pegmatites containing complex, volatile-bearing zirconium silicate minerals (the Langesundsfjord type). These pegmatites are relatively abundant in the southwestern part of the Larvik Plutonic Complex and its border zone in the Langesundsfjord archipelago and the adjoining mainland area (Fig. 1).
(3) The rare, agpaitic Bratthagen type pegmatites with parakeldyshite (Na_2ZrSiO_7), lorenzenite ($Na_2Ti_2Si_2O_9$) and dalyite ($K_2ZrSi_6O_{15}$) are associated with foyaite rather than larvikite, and restricted to a small area in the northern part of the complex (Larsen, 2010, and references therein).

The Langesundsfjord type pegmatites are intrusive in nepheline-normative larvikite belonging to ring segment VI, and in contact-metamorphosed, Permo-Carboniferous basalt (Fig. 1). Pegmatites in this area occur as more or less irregular veins, often not particularly coarse-grained. The main minerals are white or greyish microcline, nepheline (often more or less altered to 'spreustein', i.e. aggregates of pink, fibrous natrolite), albite ± sodalite ± aegirine ± ferro-edenite (barkevikite) ± magnetite ± biotite. Fluorite is a common mineral in these pegmatites, pyrophanite ($MnTiO_3$) is also relatively common, ilmenite and rutile much less so (Larsen, 2010). In addition, a large variety of accessory minerals may be present, and the abundance of Zr-, Ti-, Nb-, rare earth element- (REE-) and Be-minerals is conspicuous (Brøgger, 1890; Larsen, 1996, 2010). The main rock-forming minerals and the zirconium silicates formed during the magmatic crystallization stage in the pegmatites. A subsequent, hydrothermal stage of evolution is discernible in most nepheline syenite pegmatites. This stage is usually characterized by extensive zeolitization and alteration of the magmatic minerals, and by crystallization of low-temperature hydroxides and hydrous silicates. Many of the rare REE- and beryllium-bearing minerals belong to this stage of pegmatite formation. A few minerals (e.g. goethite, hisingerite, neotocite) have formed as the result of supergene processes (Larsen, 2010). The present study is concerned only with the first, magmatic stage of pegmatite crystallization. The host larvikite crystallized at shallow-crustal pressures ($P \approx 1$ kbar), and reached its solidus at 850–860°C (Neumann, 1976, 1980), which defines the maximum pressure and temperature for emplacement of the pegmatites. From the compositions of coexisting Fe–Ti oxides, Neumann (1976) determined a consistent T–f_{O2} cooling trend for the Larvik Plutonic Complex parallel to and less than one log f_{O2} unit below the quartz–fayalite–magnetite (QFM) buffer curve; oxygen fugacity was buffered by equilibria involving silicate melt, Fe–Ti oxides and mafic silicate minerals during crystallization of the pluton.

PETROGRAPHY

In addition to samples collected for this study, *c.* 180 samples of nepheline syenite pegmatite in the mineral collections of the Natural History Museum, University of Oslo, and the National Museum of Natural History (NRM), Stockholm, Sweden were examined under the binocular microscope, and visual mineral identifications were checked by X-ray diffraction (XRD) on selected specimens (Electronic Appendix 1, available at http://www.petrology.oxfordjournals.org). The Stockholm collection is of special interest, as it contains many of the samples first studied by Brøgger (1890). Detailed scanning electron microscopy and electron microprobe work was done on samples from selected pegmatites indicated in Fig. 1. Descriptions of the samples analysed by electron microprobe in the present study are given in Electronic Appendix 2, at http://www.petrology.oxfordjournals.org.

Some of the samples examined in this study are pegmatitic in the classical sense; that is, ultra-coarse-grained rocks with well-developed crystals of the rock-forming minerals. Others, however, are medium- to coarse-grained intrusive magmatic rocks, many of which are heterogeneous in terms of grain size and mineralogy on a hand-specimen scale.

Fluorite has been observed in most samples examined in this study, occurring in two textural settings (Fig. 2, Table 2). In most samples it occurs as part of the early, magmatic mineral assemblage, forming intergrowths with and primary inclusions in the Zr-silicate minerals (Fig. 2h and k). However, fluorite also occurs in younger, crosscutting veins (Fig. 2l) and in symplectites replacing zirconium

silicate minerals (Fig. 2b). Zircon and the other zirconium silicate minerals commonly occur as euhedral to subhedral crystals with well-developed crystal face terminations against matrix feldspar, nepheline and sodalite, or they are included in or intergrown with biotite and/or pyroxene.

Occurrence and textural relationships of the zirconium silicate minerals

Hiortdahlite forms plate-shaped crystals with pale yellow to greyish or brownish yellow colour (Fig. 2a). It is commonly in contact with or intergrown with fluorite and the groundmass minerals microcline, nepheline and aegirine; in samples TRO, RIS and ARS also with rosenbuschite (Fig. 2f). Sample 24102 from the Langodden pegmatite contains euhedral plates of hiortdahlite in contact with zircon (Fig. 2a), and hiortdahlite in sample ARS contains primary inclusions of zircon. In hiortdahlite-bearing samples also containing eudialyte, the two minerals occur in direct contact. In sample ARS, hiortdahlite also occurs as primary inclusions in pyroxene. Hiortdahlite contains primary inclusions of nepheline, microcline, apatite, fluorite, wöhlerite and tritomite-(Ce). Alteration products of hiortdahlite include zircon + fluorite intergrowths along grain boundaries (Fig. 2b), catapleiite (Fig. 2c) and låvenite–rosenbuschite (Fig. 2h) intergrowths along crosscutting fractures.

Wöhlerite occurs as aggregates of plate-shaped, bright yellow crystals, intergrown with biotite and enclosed by feldspar and nepheline. Samples containing wöhlerite commonly contain only small amounts of late or secondary fluorite, or are free of visible fluorite, unless the samples also contain eudialyte *sensu lato* (*s.l.*), hiortdahlite and/or rosenbuschite. Where fluorite is found spatially associated with wöhlerite, it either fills fractures associated with incipient alteration (Fig. 2l), or it occurs in aggregates together with hiortdahlite and/or rosenbuschite replacing wöhlerite, or it is in a clearly interstitial textural position with respect to wöhlerite. Wöhlerite occurs as primary inclusions in hiortdahlite (Fig. 2b) and låvenite (Fig. 2j), and contains primary inclusions of pyrochlore (Fig. 2l). Direct contacts between wöhlerite and eudialyte have been observed in sample TRO.

Låvenite forms aggregates of orange–brown, subhedral to anhedral grains in a matrix consisting of alkali feldspar, nepheline, biotite and clinopyroxene. It contains inclusions of wöhlerite and pyrochlore (Fig. 2j), and in sample LV10, it forms primary intergrowths with fluorite (Fig. 2k). In sample LV15, a låvenite-like mineral has formed along the boundary between wöhlerite and a cross-cutting fluorite vein (Fig. 2l). In sample TRO, a BSE-bright låvenite has formed by alteration of hiortdahlite (Fig. 2h), and in sample ARS, intergrowths of fluorite and a låvenite-like mineral form patches in eudialyte (Fig. 2e). At Låven, låvenite has been replaced by symplectites consisting of fluorite, magnetite and zircon (Fig. 2k, arrows); according to Brøgger (1890), this type of alteration is common for låvenite in the area.

Rosenbuschite typically forms pale, acicular crystals intergrown with hiortdahlite (Fig. 2f) and eudialyte (Fig. 2g); in sample TRO, it replaces hiortdahlite (Fig. 2h). Rosenbuschite is closely associated with fluorite, which is a general observation in these pegmatites (Brøgger, 1890; Larsen, 2010). The type specimen (TYROS, NRM no. 531136) shows distinct, patchy variations in BSE brightness, suggesting compositional heterogeneity (Fig. 2d).

Eudialyte in these pegmatites typically has a brown or orange–brown colour, and occurs as anhedral masses in contact with or enclosing rosenbuschite, hiortdahlite and låvenite (Fig. 2g). As pointed out by Brøgger (1890), zircon is not found in primary coexistence with eudialyte, but it does occur as an alteration product in eudialyte-bearing samples.

Catapleiite commonly belongs to a late magmatic stage of evolution in the pegmatites (Larsen, 2010). However, in the present samples it occurs both as primary inclusions in hiortdahlite (sample IGH from Stokksund), and as an alteration product after hiortdahlite (Fig. 2c). Samples from the Låven pegmatite and sample 30047 from Vesle Arøya contain both låvenite and catapleiite, but the two minerals have not been found in direct grain contact.

Other minerals occurring in intergrowths with the zirconium silicate minerals or as primary solid inclusions are apatite (Fig. 2g), tritomite-(Ce), monazite (Fig. 2i), Ca-free REE silicate minerals, and pyrochlore (Fig. 2j and l).

MINERAL CHEMISTRY

Analytical methods

Scanning electron microscopy and electron microprobe (EMP) analysis was carried out at the Department of Geosciences, University of Oslo, and XRD at the Natural History Museum, University of Oslo. Mineral fragments for XRD and electron microprobe work were separated from the pegmatite matrix under a binocular microscope; samples for EMP analysis were mounted in epoxy and polished. The samples were imaged using backscattered electrons on a Cameca SX100 electron microprobe and a JEOL JSM 6460LV scanning electron microscope with an Oxford Instruments LINK INCA energy dispersive analyser prior to and during the analytical sessions, the BSE images acting as guides for the selection of points to be analysed.

Electron microprobe analysis was performed on a Cameca SX100 fitted with five wavelength-dispersive

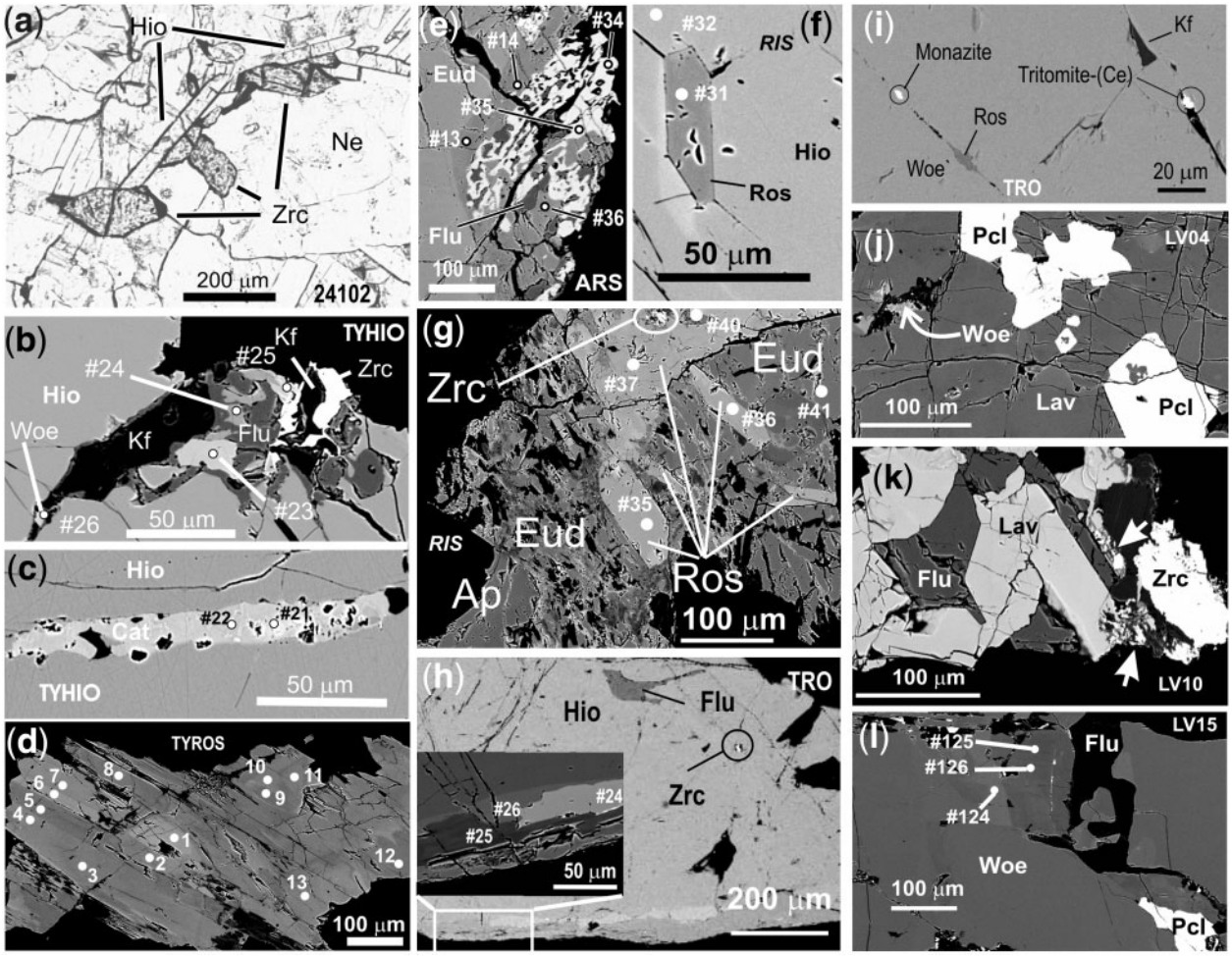

Fig. 2. Microstructural relationships of zirconium silicate minerals in nepheline syenite pegmatites from the Larvik Plutonic Complex. The terms 'primary' and 'secondary' inclusions are used in the sense commonly used in the fluid inclusion literature, referring to inclusions trapped during crystal growth, and along healed fractures in the host mineral, respectively (e.g. Roedder, 1984). Numbered points on the images represent electron microprobe analyses listed in Electronic Appendix 3. (a) Polarized light photomicrograph of pegmatite sample 24102 from Langodden (locality 3 in Fig. 1). Elongated plates of hiortdahlite (*Hio*) and stubby prisms of zircon (*Zrc*) in mutual contact embedded in a matrix of alkali feldspar (anhedral grains with visible cleavage) and nepheline (*Ne*). (b) EMP-BSE image of a fragment of the hiortdahlite holotype (TYHIO from the Langodden pegmatite, locality 3 in Fig. 1), showing primary inclusions of microcline (*Kf*) and wöhlerite (*Woe*) in hiortdahlite, and aggregate of zircon (*Zrc*) and fluorite (*Flu*) formed at the grain boundary of hiortdahlite by post-crystallization processes. (c) Secondary catapleiite (*Cat*) along a healed fracture in hiortdahlite from the hiortdahlite holotype (TYHIO). Dark spots within the catapleiite vein are cavities limited by crystal faces (i.e. fluid inclusions cross-cut by the section surface). (d) A grain of the rosenbuschite holotype analysed in the present study (TYROS from Skutesundskjær, locality 1 in Fig. 1). The patchy variations in BSE intensity are due to minor variations in Ti/(Ti + Zr + Hf) ratio of the rosenbuschite (Fig. 3c and Electronic Appendix 3). (e) An intergrowth of a BSE-bright, låvenite-like mineral ('low-Fe låvenite') and BSE-dark fluorite (*Flu*) enclosed by eudialyte (*Eud*). Eudialyte shows lower BSE brightness next to the aggregate. Sample ARS from Arøyskjærene (locality 4 in Fig. 1). (f) A grain of hiortdahlite (*Hio*) from the Risøya pegmatite (locality 5 in Fig. 1), with a cross-section through an euhedral fibre of rosenbuschite (*Ros*) occurring as a primary inclusion in hiortdahlite. (g) An aggregate consisting of eudialyte (*Eud*), rosenbuschite (*Ros*) and apatite (Ap) from the Risøya pegmatite (locality 5 in Fig. 1). Minor zircon (*Zrc*) is fracture-bound and probably formed by alteration of rosenbuschite. (h) Hiortdahlite (*Hio*) from the Trompetholmen pegmatite (locality 6 in Fig. 1) with primary inclusions of zircon (*Zrc*) and fluorite (*Flu*). Black inclusions are alkali feldspar. The inset detail shows alteration of hiortdahlite to a låvenite-like mineral ('low-iron låvenite', analysis 24) and rosenbuschite (analysis 25) along a secondary healed fracture. Analysis 26 is a hiortdahlite with slightly higher Zr/(Ti + Zr) than the BSE-darker hiortdahlite away from the fracture (Electronic Appendix 3). The BSE contrast of the enlarged inset has been enhanced. (i) Wöhlerite (*Woe*) from the Trompetholmen pegmatite (locality 6 in Fig. 1) with inclusions of microcline (*Kf*), monazite and tritomite-(Ce), which appear to be primary in the wöhlerite, whereas monazite and rosenbuschite (*Ros*) are located at a healed fracture trail, and are due to secondary mineral–fluid interaction processes at the late- or post-magmatic stage. (j) Homogeneous låvenite (*Lav*) in sample LV04 from the Låven pegmatite (locality 7 in Fig. 1) with primary inclusions of wöhlerite (*Woe*) and pyrochlore (*Pcl*). (k) Låvenite (*Lav*) intergrown with fluorite (*Flu*) in sample LV10 from the Låven pegmatite. Zircon (*Zrc*) is a secondary mineral in this sample, probably belonging to a stage of hydrothermal recrystallization at late- or post-magmatic conditions. Near the zircon crystal, låvenite is replaced by symplectites (arrows) consisting of zircon (BSE-bright) and fluorite (BSE-dark). (l) Wöhlerite (*Woe*) with a primary inclusion of pyrochlore (*Pcl*) in sample LV15 from the Låven pegmatite. The wöhlerite is penetrated by a fluorite vein (*Flu*), against which wöhlerite is rounded and resorbed, and locally replaced by a låvenite-like mineral ('low-Fe låvenite', analyses 125 and 126). 'Low-iron låvenite' and wöhlerite show very similar BSE brightness, and can be distinguished only from electron microprobe analyses (Electronic Appendix 3).

Table 2: Summary of critical mineral assemblages in pegmatites from the Larvik Plutonic Complex

Locality	Fig. 1[1]	Sample	Mineral assemblages	
			Magmatic stage	Late or secondary stage
Langodden	3	TYHIO	a_1: Wöhlerite + hiortdahlite	
			a_2: Hiortdahlite + zircon + fluorite	a_3: Zircon + fluorite ± catapleiite
Vesle Arøya	8	30047	*b*: Låvenite + eudialyte/catapleiite[2]	
Trompetholmen	6	TRO	c_1: Wöhlerite + pyrochlore + eudialyte ± zircon	
			c_2: Hiortdahlite + rosenbuschite + eudialyte + fluorite	c_3: Low-Fe låvenite + fluorite
Risøya	5	RIS	d_1: Wöhlerite + eudialyte	d_3: Zircon + fluorite
			d_2: Hiortdahlite + rosenbuschite + eudialyte + fluorite	
Arøyskjærene	4	ARS	e_1: Zircon + fluorite	
			e_2: Hiortdahlite + rosenbuschite + eudialyte + fluorite	e_3: Catapleiite + zircon + fluorite
Skutesundsjkjær	1	TYROS	*f*: Rosenbuschite + fluorite	
	1	30086	g_1: Wöhlerite + pyrochlore	
			g_2: Hiortdahlite + rosenbuschite + fluorite	
Stokksund	2	IGH	*h*: Hiortdahlie + catapleite + fluorite	
Låven	7	TYLA	*i*: Låvenite	
	7	LV04	j_1: Wöhlerite	
			j_2: Låvenite + fluorite + pyrochlore	
	7	LV10	k_1: Låvenite + fluorite	k_2: Zircon + fluorite
	7	LV15	l_1: Låvenite + wöhlerite	
			l_2: Låvenite + fluorite	
	7	LV08	*m*: Catapleiite	

[1]Localities marked in Fig. 1.
[2]The paragenetic relationship between catapleiite and the other minerals is unclear.
a_1, a_2, a_3, etc.: successive mineral assemblages in the pegmatite.

(WDS) spectrometers. An accelerating voltage of 15 kV, beam current of 15 nA and a focused beam were generally used. Beam-sensitive minerals (catapleiite and eudialyte) were analyzed at 10 nA and a beam diameter of 10 μm. Counting time was 10 s on peak (and 5 s on each background positions). Na, F, Cl and K were analyzed first. Prior to analysis, full-range spectra were acquired on several grains of each mineral species to identify all the elements present and possible interferences between X-ray lines. Background positions for each mineral type were then selected on detailed WDS scans acquired around the X-ray lines of interest.

Calibration standards and X-ray lines used were wollastonite (Si Kα, Ca Kα), Al_2O_3 (Al Kα), pyrophanite (Ti Kα, Mn Kα), Fe metal (Fe Kα), MgO (Mg Kα) orthoclase (K Kα), albite (Na Kα), fluorite (F Kα), synthetic alforsite (Cl Kα), Monastery Mine zircon (Zr Lα), Hf metal (Hf Mα), Si–Al–Ca glass with 15% ThO_2 (Th Mα), Nb_2O_5 (Nb Lα), Ta_2O_5 (Ta Mα), scheelite (W Mα), synthetic orthophosphates (Jarosewich & Boatner, 1991) for REE and Y (La Lα, Ce Lα, Nd Lβ, Y Lα).

Matrix corrections were made according to the PAP procedure (Pouchou & Pichoir, 1984).

In XRD analysis, crystalline materials examined in this study were identified using a Siemens D5005 X-ray powder diffractometer equipped with a ceramic X-ray tube (2·2 kW) and a Cu-Kα-anode and Debye–Scherrer configuration, combined with BRUKER software for evaluation (EVA) with the latest PDF database. Several of the specimens in the Oslo collection were originally identified by XRD using 9 cm Debye–Scherrer cameras and Fe-Kα radiation; the films are kept in the archives of the Natural History Museum, University of Oslo.

Mineral compositions

Electron microprobe data are given in Electronic Appendix 3 (http://www.petrology.oxfordjournals.org). Hiortdahlite, wöhlerite, låvenite and rosenbuschite were recalculated to structural formulae assuming Si = 4·00 cations. This is justified by the $A_{6+x}B_{2-x}(Si_2O_7)_2(F,O,OH)_4$ stoichiometry of these minerals, but it should be noted

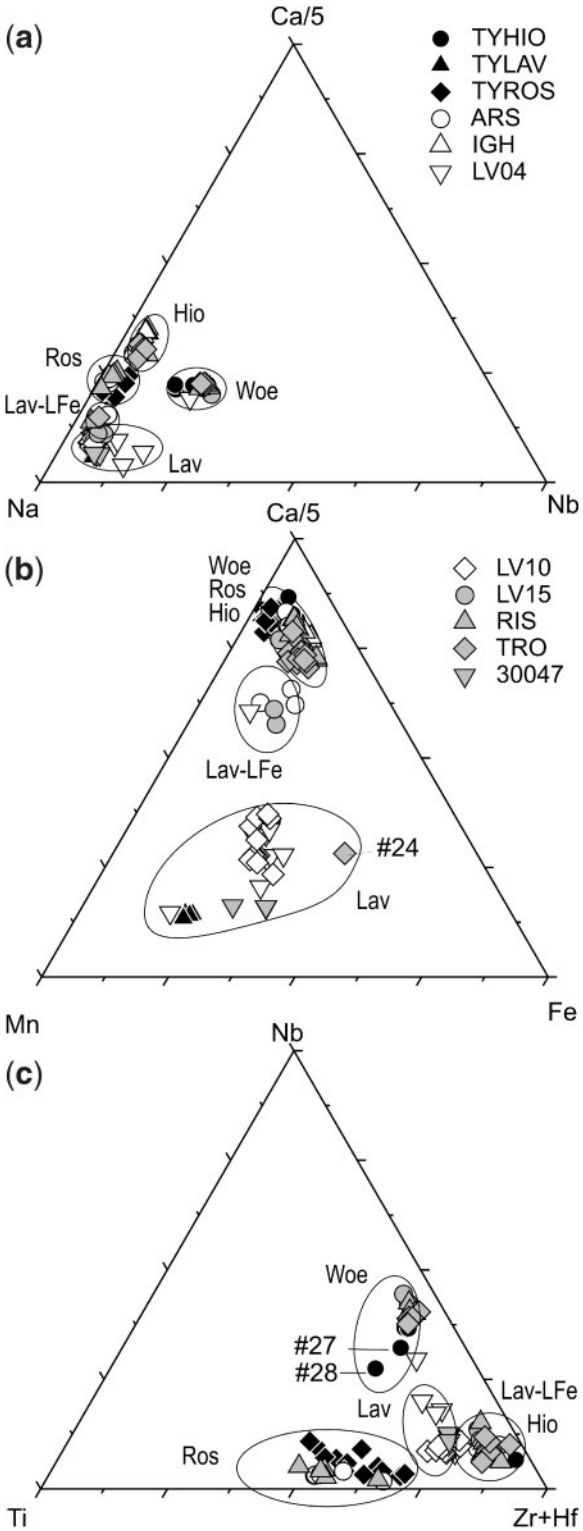

Fig. 3. Cation distribution in hiortdahlite (Hio), wöhlerite (Woe), låvenite (Lav) and rosenbuschite (Ros); data from Electronic Appendix 3. Numbers refer to analyses mentioned in the text. Analysis numbers should be combined with the appropriate sample identifier, so that the point marked '#24' in (b) corresponds to TRO analysis 24 in Electronic Appendix 3. (a) Na–Nb–Ca/5 (Keller *et al.*, 1995). It should be noted that the 'low-iron låvenite' has Na/(Ca + Na) between the compositional ranges of låvenite and rosenbuschite. (b) Mn–Fe–Ca/5. In this plot, wöhlerite, rosenbuschite and hiortdahlite cannot be distinguished, but låvenite stands out with significantly higher Fe + Mn. Noteworthy features are the range of Fe/(Fe + Mn) ratios in låvenite, and the intermediate position of the 'low-iron låvenite'. (c) Quadrivalent and pentavalent ions, represented by Ti–Zr + Hf–Nb. Wöhlerite stands out with high Nb in this diagram. (Note also the range in Ti/(Ti + Zr + Hf) in rosenbuschite, and that the rosenbuschite holotype (TYROS) show an internal compositional range corresponding to the total variation in rosenbuschite observed in the present study.)

that a minor error in the Si analysis may propagate to a significant error in the total charge balance. The minerals considered here all have Zr/Ti > 1, which distinguishes them from related, Ti-dominated species such as rinkite, hainite, kochite and mosandrite (Table 1). Ta, W and U concentrations are below the detection limit of the electron microprobe. Cl is insignificant in wöhlerite- and rosenbuschite-group minerals, but O^{2-} (and possibly OH^{-}) substitutes for fluorine in amounts ranging from ≤0·5 a.p.f.u. (atoms per formula unit) in hiortdahlite to >2·0 a.p.f.u. in wöhlerite, which accounts for a small deficiency in the analytical totals.

Wöhlerite shows little compositional variation within and between the samples. If two analyses of low-Nb–high-Ti wöhlerite inclusions in the hiortdahlite holotype (TYHIO analyses 27 and 28, Fig. 3c, Electronic Appendix 3) are excluded, the composition is given by the formula $Na_{2·0}Ca_{3·8}(Fe,Mn)_{0·3}Ti_{0·1}Zr_{1·0}Nb_{0·7}(Si_4O_{14})F_{1·8}O_{2·2}$, which is indistinguishable from published analyses of wöhlerite from the region (Brøgger, 1890; Mariano & Roeder, 1989). Wöhlerite has lower fluorine (<4·5 wt %), Na and REE concentrations, but significantly higher Nb than the other wöhlerite-group minerals analyzed in this study (Fig. 3c).

Hiortdahlite is the most calcium-rich (>30 wt % CaO) and sodium-poor member of the wöhlerite-group species analyzed here (Fig. 3a); its fluorine concentration (*c.* 8 wt %) is significantly higher than that of wöhlerite, and comparable with that of rosenbuschite. It also shows restricted compositional variation within samples, but there is a minor but probably significant difference in Na/Ca ratio between the Stokksund (IGH) sample and the hiortdahlite holotype on one hand, $(Na_{1·9}Ca_{4·4}(Fe,Mn)_{0·3}REE_{0·1}Ti_{0·1}Zr_{1·1}Nb_{0·1}(Si_4O_{14})F_{3·4}O_{0·6})$, and the Risøya, Arøyskjær and Trompetholmen hiortdahlite on the other $(Na_{1·7}Ca_{4·6}(Fe,Mn)_{0·2}REE_{0·1}Ti_{0·1}Zr_{1·1}Nb_{0·1}(Si_4O_{14})F_{3·5}O_{0·5})$.

Låvenite in TYLA and 30047 is homogeneous, with composition close to the ideal endmember at $(Na_{3·1}Ca_{1·1}(Fe,Mn)_{1·3}REE_{<0·1}Ti_{0·3}Zr_{1·8}Nb_{0·3}(Si_4O_{14})F_{2·2}O_{1·8})$. Låvenite in samples LV04 and LV10 shows much more variable composition ranging towards *c.* $Na_3Ca_2(Fe,Mn)_{0·7}$

$Ti_{0.3}\mathcal{Z}r_{1.8}Nb_{0.2}(Si_4O_{14})F_{3.5}O_{0.5}$, and higher Fe/(Fe + Mn) ratio (Fig. 3b). The overall compositional variations of låvenite in these samples are controlled by simple $FeMn_{-1}$ and $Ca_{-1}(Mn,Fe)$ substitutions, and a coupled cation–anion substitution of the type $CaF_2M^{4+}{}_{-1}O_{-2}$, where M^{4+} is Zr, Hf and Ti (Fig. 3b and c).

The BSE-bright alteration product in hiortdahlite from Trompetholmen (TRO analysis 24, Fig. 2h) is låvenite with higher Fe/Mn ratio than any of the other låvenites analysed (Fig. 3b). The BSE-bright mineral in hiortdahlite from Risøya (RIS analysis 33), the alteration zone in wöhlerite against fluorite in LV15 (LV15 analyses 124 and 125), and the BSE-bright phase intergrown with fluorite in the symplectite-like patches in Arøyskjærene eudialyte (ARS analyses 34, 35, 39, Fig. 2e) all have compositions clustering around an idealized composition $Na_3Ca_{2.5}(Fe,Mn)_{0.3}Ti_{0.2}\mathcal{Z}r_{1.8}Nb_{0.2}(Si_4O_{14})F_{3.5}O_{0.5}$, which falls within the compositional gap between låvenite and rosenbuschite, hiortdahlite and wöhlerite (Fig. 3). The observed compositions are compatible with Si_2O_7 type structures of rosenbuschite or wöhlerite type; the low Ti suggests that they belong in the wöhlerite group rather than in the rosenbuschite group (Fig. 3c). This composition is most similar to låvenite, but has lower Fe + Mn and higher Ca than any låvenite reported in literature, including the yellow låvenite from Vesla Arøya analysed by Friis *et al.* (2010). Below, it will be referred to as 'low-iron låvenite'.

Rosenbuschite contains Ti as an essential component in its structure, and the new analyses of the mineral show consistently higher Ti concentrations than in the coexisting wöhlerite group minerals. It is also more variable in composition than wöhlerite and hiortdahlite. The new analyses correspond to an approximate range in major components from $Na_{2.2}Ca_{3.8}(Fe,Mn)_{0.2}REE_{0.2}Ti_{0.7}\mathcal{Z}r_{0.9}Nb_{0.1}(Si_4O_{14})F_{3.2}O_{0.8}$ to $Na_{2.6}Ca_{3.3}(Fe,Mn)_{0.1}REE_{0.1}Ti_{0.6}\mathcal{Z}r_{1.2}Nb_{0.1}(Si_4O_{14})F_{3.2}O_{0.8}$. Simple $(\mathcal{Z}r,Hf)Ti_{-1}$ substitution and a coupled $Na_2M^{4+}Ca_{-3}$ are the main controls on th compositional variation. An overall variation in F from 2·5 to 3·5 a.p.f.u. is uncorrelated with Ca. The sample of the rosenbuschite holotype (TYROS) is compositionally heterogeneous, with an internal variation in Zr + Hf and (Zr + Hf)/Ti ratio comparable with the total compositional variation of the rosenbuschite samples analysed in this study (Fig. 3c). The variation in the (Zr + Hf)/Ti ratio is qualitatively correlated with patchy variations in BSE intensity shown in Fig. 2d. The analysis of the same sample reported by Christiansen *et al.* (2003) falls in the middle of the range of the new analyses.

The minerals of the eudialyte group have complex structures based on three- and nine-membered rings and single SiO_4 groups (Johnsen *et al.*, 2003).The general formula can be written $[N(1)N(2)N(3)N(4)N(5)]_3[M(1a)M(1b)]_3M(2)_3M(3)M(4)\mathcal{Z}_3[Si_{24}O_{72}]O_4X_2$, in which X = Cl, F, OH or CO_3, $\mathcal{Z}$ = Zr + Ti, and N and M are cation sites incorporating Na, K, Ca, Nb, Fe, Mn (Johnsen *et al.*, 2003). Si is also accommodated in the off-ring, tetrahedral position *M4*, and it competes with Nb and other high-valence ions in four- to six-coordinated *M3* position. The compositions of eudialyte *s.l.* in Electronic Appendix 3 have been recalculated to a constant sum of Si + Al + Nb + Zr + Hf + Ti = 29·000 (Johnson & Grice, 1999), and cation distributions have been calcualted using the algorithm of Pfaff *et al.* (2010), modified so that excess Ca + REE is allocated to the *N* sites irrespective of other site occupancies. The eudialyte *s.l.* analysed in this study has total Fe/Mn > 1 (Fig. 4a). Most analyses have $Si_{M3}/Nb_{M3} \approx 1$, and incorporate minor Ti + Zr in *M3* (Fig. 4b). $\mathcal{Z}$ is filled by Zr + Hf, and *M2* is fully occupied by Fe and Mn, with excess Mn in *M1*, which is otherwise dominated by Ca. The *N* positions hold Na, K, Ca and REE, with total *N*-site occupancy ≤14·6 cations. The distribution of cations in the *M3* and *N* sites indicates that the eudialyte *s.l.* in these pegmatites can best be described as a feklichevite–ferrokentbrooksite–zirsilite–eudialyte solid solution with $H_3O^+{}_N$ and/or vacancies relative to 16 *N*-positions (Fig. 4c and d; endmembers from Johnsen *et al.*, 2003). Eudialytes from other pegmatites in the Larvik Plutonic Complex have been classified as intermediates between ferrokentbrooksite and zirsilite (Larsen *et al.*, 2005*a*, 2005*b*). The name 'eudialyte' is, however, retained in the following discussion. Chlorine amounts to between 0·75 and 1·40 wt %, but the combined amount of Cl and F will not fill the *X* positions, indicating additional substitution of OH or CO_3 in these positions, in agreement with the low sums.

In eudialyte from the Arøyskjærene pegmatite, BSE-dark zones rimming aggregates of fluorite and low-iron låvenite (Fig. 2e) show simultaneous reduction of Na and Ca, slightly increasing cation deficiency and increasing $[Na/(Na + Ca)]_N$ towards the aggregates (compare points for ARS analyses 36, 13 and 14 from the intergrowth zone shown in Fig. 2e with those for ARS analyses 11, 12, 33 and 32 from the central part of the same grain). The most likely explanation for the reduced BSE brightness in these zones is increasing substitution of water in the eudialyte.

Catapleiite is a water-bearing silicate whose structure is based on Si_3O_9 rings (Table 1). The present analyses (Electronic Appendix 2) range from a pure sodium catapleiite ($Na_2\mathcal{Z}rSi_3O_9{\cdot}2H_2O$) to a composition close to $NaCa_{0.5}\mathcal{Z}rSi_3O_9{\cdot}2H_2O$), controlled by the vacancy substitution mechanism $Ca\square Na_{-2}$. This range of composition mimics that reported by Larsen (2001) for catapleiite from the Larvik Plutonic Complex. Catapleiite in LV08 is distinctly cation deficient at a composition $Na_{0.6}Ca_{0.3}\mathcal{Z}rSi_3O_9{\cdot}2H_2O$.

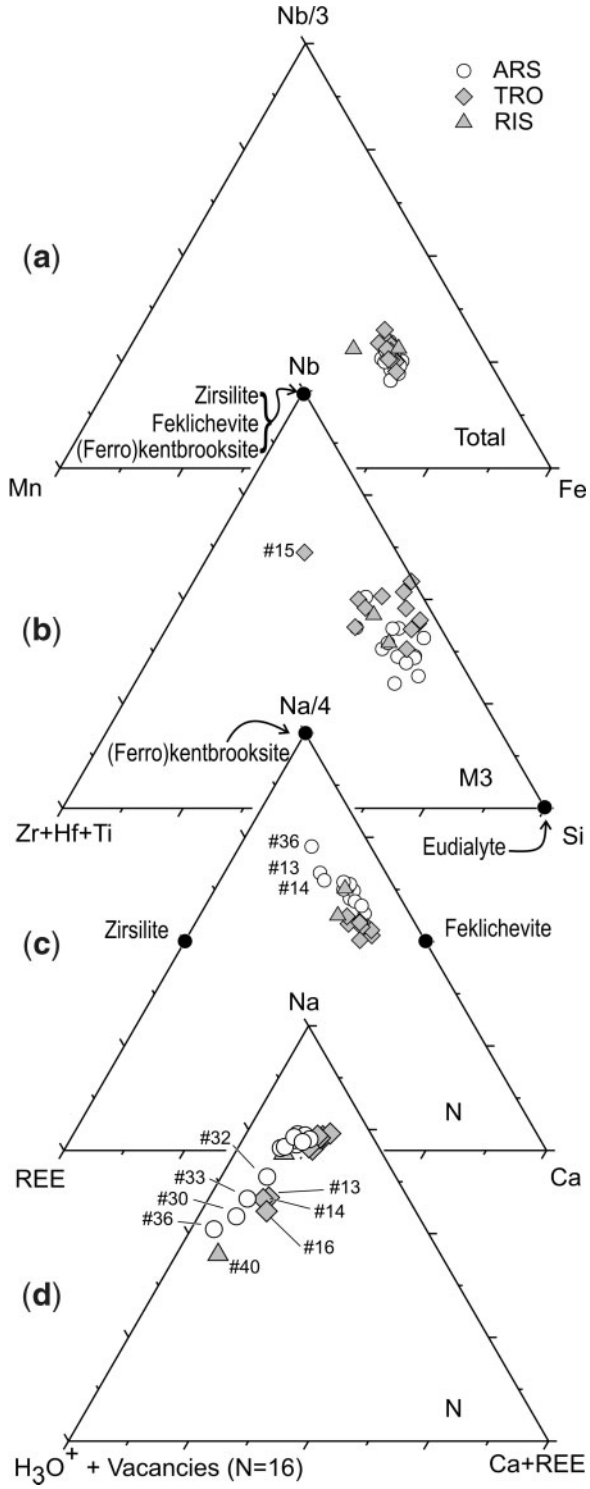

Fig. 4. Cation distributions in eudialyte *s.l.*, from data given in Electronic Appendix 3. Structural formulae have been calculated assuming Si + Al + Ti + Zr + Hf + Nb = 29·000; cations have been assigned to structural positions as given by Johnsen *et al.* (2003) using an adaptation of the algorithm of Pfaff *et al.* (2010), which allows excess Ca + REE to be allocated to the *N*-positions in the structure without regard for other site occupancies. Endmember compositions indicated by black dots have been taken from table 3 of Johnsen *et al.* (2003). (a) Total Mn–Fe–Nb distribution, illustrating that Fe > Mn in eudialyte in these samples. (b) *M3* cation distribution, showing roughly equal Nb and Si occupancies in this position. (c) *N*-cation distribution, illustrating the significant contribution of Ca + REE in eudialyte from these pegmatites. (d) Vacant and occupied *N*-positions, shown in a Na_N–$(Ca + REE)_N$–$(H_3O^+ + \square)_N$ diagram. The sum of vacancies and H_3O^+ ions in the *N* position has been estimated assuming 16 N-positions.

MODELLING THE STABILITY OF ZIRCONIUM SILICATE LIQUIDUS ASSEMBLAGES IN PERALKALINE NEPHELINE SYENITE MAGMA

Primary and secondary zirconium silicate mineral assemblages

The minerals of the wöhlerite, rosenbuschite and eudialyte groups are part of the magmatic mineral assemblage of the pegmatites, together with the main rock-forming minerals microcline, albite, annite-rich biotite, aegirine/aegirine–augite, magnetite, fluorite and minor and accessory minerals (pyrochlore, apatite, tritomite-(Ce) and others). Based on the present observations, sequences of successive mineral assemblages related to magmatic and post-magmatic processes can be established (Table 2). An assemblage is identified by a lower-case letter representing the sample, and a subscript number giving the relative timing of the assemblage in the crystallization history of that particular sample. For example, the Langodden pegmatite shows three successive zirconium silicate mineral assemblages: early crystallized wöhlerite and hiortdahlite (assemblage a_1 in Table 2) was followed first by hiortdahlite and zircon (a_2), and later by secondary assemblages with zircon, fluorite and catapleiite (a_3).

Hiortdahlite, rosenbuschite, låvenite and zircon form part of primary mineral assemblages with magmatic fluorite (assemblages a_2, c_2, d_2, f, g_2, h, j, k_1), but there is no evidence for equilibrium coexistence of wöhlerite with fluorite. Wöhlerite does, however, occur in magmatic assemblages with eudialyte at Risøya and Trompetholmen (assemblages c_1 and d_1), with hiortdahlite at Langodden (a_1), with pyrochlore at Skutesundskjær (g_1) and låvenite at Låven (l_1). Inclusions of rosenbuschite observed in wöhlerite appear to be trail-bound and secondary (Fig. 2i). In the samples from Trompetholmen and Risøya, wöhlerite (assemblages c_1, d_1) and hiortdahlite + rosenbuschite (assemblages c_2, d_2) occur in separate domains, which may record different stages of crystallization or small-scale heterogeneity in composition. Replacement of wöhlerite by assemblages with fluorite and hiortdahlite and/or rosenbuschite is a common feature in wöhlerite-bearing pegmatites (Table 2), suggesting that the wöhlerite + eudialyte and hiortdahlite + eudialyte + fluorite ± rosenbuschite assemblages reflect successive stages of magmatic crystallization.

Zircon forms part of early mineral assemblages in the Langodden and Arøyskjærene pegmatites (a_2, e_1). Secondary fluorite + zircon ± catapleiite assemblages are found in several of the samples studied (assemblages a_3, d_3, e_3, k_2; Table 2). Other late magmatic or secondary assemblages are made up by fluorite + low-iron låvenite (assemblage c_3), replacing hiortdahlite in the Trompetholmen pegmatite (Fig. 2h) and wöhlerite in LV15 (assemblage k_2, Fig. 2l). Låvenite is itself commonly replaced by pseudomorphs consisting of zircon, fluorite and magnetite, which must have formed during a later, post-magmatic stage of evolution (Fig. 2k). The textural status of the symplectite-like aggregates of fluorite and the BSE-bright zirconium silicate mineral in the Arøyskjærene eudialyte (Fig. 2e) is enigmatic, but the observation that eudialyte is increasingly Na + Ca deficient and hydrated towards the contact to the aggregates suggests that this feature is due to interaction with an aqueous fluid, and that the aggregates are pseudomorphs after hiortdahlite or rosenbuschite. Although catapleiite forms part of the liquidus assemblage in some pegmatites, it also occurs in late replacement assemblages together with zircon and fluorite in others (Table 2).

Chemographic analysis

The magmatic mineral assemblages including zirconium silicates and the main rock-forming minerals of the pegmatites are related to the silicate liquid by a series of mineral–melt reactions that are influenced by parameters such as temperature, pressure, oxygen fugacity, activities of volatile species (e.g. water and halogens), and the peralkalinity of the melt. In the present study, we assume crystallization at constant pressure and temperature for the magmatic stage, and evaluate the relative influence on mineral stability of the excess alkali content of the melt (represented by the activity of the sodium disilicate component, $Nds = Na_2Si_2O_5$, e.g. Andersen & Sørensen, 2005) and the activities of water, fluorine and chlorine (represented by HF and HCl). The composition-dependent variables a_{Nds}, a_{HF} and a_{H_2O} define a 3D chemical potential or log activity space in which a petrogenetic grid can be constructed from observed mineral assemblages and compositions using the Schreinemakers method (Zen, 1966; White *et al.*, 2008, and references therein).

Twenty or more components are necessary to give a full chemographic description of the zirconium silicate-bearing mineral assemblages of the pegmatites. This is clearly not possible, and some simplifications must be made. The number of components can be reduced by elimination of minor species by combining Hf with Zr, Y with the REE, and Mn and Mg with Fe. The pertinent mineral reactions can then be modelled in terms of the simplified 11 oxide components $NaO_{0·5}$, $KO_{0·5}$, CaO, FeO, $REEO_{1·5}$, ZrO_2, TiO_2, $NbO_{2·5}$, $AlO_{1·5}$, SiO_2, $HO_{0·5}$ and two volatile exchange components: $FO_{-0·5}$ and $ClO_{-0·5}$. By omitting ferric iron from the system, we disregard the effect of oxygen fugacity. In these pegmatites, f_{O2} is, however, internally controlled by reactions involving titanomagnetite, microcline and biotite.

Stoichiometric endmember compositions for the major rock-forming minerals microcline, albite, nepheline and sodalite are used in the model calculations (Table 3). Micas in the pegmatites are close to annite in composition (Larsen, 1998), and we include a pure hydroxy annite endmember in our calculations, assuming the F–Fe avoidance principle in biotite (Munoz, 1984) to be applicable. Clinopyroxene in the nepheline syenite pegmatites is in general aegirine–augite to aegirine; *c.* 10 mol % of the hedenbergite ($CaFeSi_2O_6$) component has been reported from the Låven and Arøyskjærene pegmatites (Larsen & Raade, 1997; Murad, 2006). Because the $NaFe^{3+}Si_2O_6$ component cannot be accounted for in the present model, we use the hedenbergite component in the calculations. This will invoke an activity term, which is, however, the same for all reactions involving pyroxene.

Niobium is essential in wöhlerite, and occurs as a minor component in rosenbuschite, hiortdahlite, låvenite and eudialyte. The main niobium (and tantalum) host in the pegmatites is, however, pyrochlore. Pyrochlore in the samples studied is metamict and altered, and we have therefore not carried out systematic analyses of this mineral. We use a theoretical endmember composition ($NaCaNb_2O_6F$) for modelling purposes.

Titanium is present in minor amounts in all of the wöhlerite and eudialyte group minerals, and is an essential structural constituent in the rosenbuschite group (Sokolova, 2006). Ti is buffered by titanomagnetite and other Ti-bearing minerals, and is ultimately related to oxygen fugacity. Here, we assume that it is externally buffered by titanium-bearing oxides (titanomagnetite, pyrophanite) and silicates (mosandrite, rinkite, astrophyllite). We also assume external buffering for the REE, which are hosted in minerals such as apatite, monazite, tritomite-(Ce) and other REE silicate minerals (Larsen, 1996), some of which contain major components not accounted for in the 13-component system (phosphorus, boron).

Chlorine is of interest only for reactions involving eudialyte. In general, an elevated activity of chlorine will increase the stability field of eudialyte at the expense of the wöhlerite and rosenbuschite group minerals. Saturation with sodalite represents the maximum attainable chloride activity of a nepheline syenite magma, and the stability field of eudialyte will therefore have a maximum size in a system crystallizing sodalite + nepheline (reaction (2) in Table 4). The highest possible activity of fluorine (or HF) is given by saturation with fluorite. The fluorite saturation reaction is divariant in the eight-component sub-system $NaO_{0·5}$–$KO_{0·5}$–CaO–FeO–$AlO_{1·5}$–SiO_2–$HO_{0·5}$–$FO_{-0·5}$

Table 3: Composition (in moles per formula unit) of phases and species used in modelling

		SiO_2	$AlO_{1.5}$	ZrO_2	TiO_2	$NbO_{2.5}$	$REEO_{1.5}$	FeO	CaO	$NaO_{0.5}$	$KO_{0.5}$	$HO_{0.5}$	$FO_{-0.5}$	$ClO_{-0.5}$
Major minerals in pegmatite														
Albite	Ab	3·0	1·0	0·0	0·0	0·0	0·0	0·0	0·0	1·0	0·0	0·0	0·0	0·0
Nepheline	Ne	4·0	4·0	0·0	0·0	0·0	0·0	0·0	0·0	3·0	1·0	0·0	0·0	0·0
Microcline	Kf	3·0	1·0	0·0	0·0	0·0	0·0	0·0	0·0	0·0	1·0	0·0	0·0	0·0
Annite component in biotite	Ann_{bi}	3·0	1·0	0·0	0·0	0·0	0·0	3·0	0·0	0·0	1·0	2·0	0·0	0·0
Hedenbergite component in clinopyroxene	Hd_{cpx}	2·0	0·0	0·0	0·0	0·0	0·0	1·0	1·0	0·0	0·0	0·0	0·0	0·0
Pyrochlore	Pcl	0·0	0·0	0·0	0·0	2·0	0·0	0·0	1·0	1·0	0·0	0·0	1·0	0·0
Sodalite	Sod	3·0	3·0	0·0	0·0	0·0	0·0	0·0	0·0	4·0	0·0	0·0	0·0	1·0
Fluorite	Flu	0·0	0·0	0·0	0·0	0·0	0·0	0·0	1·0	0·0	0·0	0·0	2·0	0·0
Zirconosilicate minerals														
Wöhlerite[1]	Woe	4·0	0·0	1·0	0·2	0·7	0·0	0·2	3·8	2·0	0·0	0·0	1·8	0·0
Rosenbuschite[1]	Ros	4·0	0·0	1·0	0·7	0·1	0·1	0·2	3·6	2·4	0·0	0·0	3·0	0·0
Hiortdahlite[1]	Hio	4·0	0·0	1·1	0·1	0·1	0·1	0·3	4·5	1·8	0·0	0·0	3·4	0·0
Låvenite[1]	Lav	4·0	0·0	1·6	0·3	0·2	0·0	0·8	1·8	3·0	0·0	0·0	2·6	0·0
Eudialyte[1]	Eud	25·4	0·1	3·1	0·1	0·4	0·6	3·6	6·9	10·5	0·2	2·0	0·2	1·1
Catapleiite[1,2]	Cat	3·0	0·0	1·0	0·0	0·0	0·0	0·0	0·3	1·4	0·0	4·0	0·0	0·0
Zircon	Zrc	1·0	0·0	1·0	0·0	0·0	0·0	0·0	0·0	0·0	0·0	0·0	0·0	0·0
Externally buffered minor oxide components														
	TiO_2	0·0	0·0	0·0	1·0	0·0	0·0	0·0	0·0	0·0	0·0	0·0	0·0	0·0
	REE_2O_3	0·0	0·0	0·0	0·0	0·0	2·0	0·0	0·0	0·0	0·0	0·0	0·0	0·0
Components in melt/fluid														
$Na_2Si_2O_5$	Nds	2·0	0·0	0·0	0·0	0·0	0·0	0·0	0·0	2·0	0·0	0·0	0·0	0·0
	H_2O	0·0	0·0	0·0	0·0	0·0	0·0	0·0	0·0	0·0	0·0	2·0	0·0	0·0
	HF	0·0	0·0	0·0	0·0	0·0	0·0	0·0	0·0	0·0	0·0	1·0	1·0	0·0

[1]Mineral compositions from Electronic Appendix 1.
[2]Additional data from Larsen (2001).

(reaction (1) in Table 4), and thus independent of which zirconium silicate minerals are stable.

Whereas there is compelling evidence for the presence of a free, aqueous fluid phase during the later, miarolitic and hydrothermal stages of pegmatite crystallization (Brøgger, 1890; Larsen, 2010), this is commonly not the case during initial, magmatic crystallization of agpaitic nepheline syenite magma (Sørensen, 1997), and we do not invoke the presence of a separate non-silicate fluid in the following analysis of magmatic phase reactions. It should, however, be noted that Brøgger (1890) observed abundant two-phase aqueous(?) fluid inclusions in catapleiite. No systematic search for fluid inclusions has been made in the present study, but observations of crystal-face limited microcavities in catapleiite in some samples (Fig. 2c) support the hypothesis that at least some of the late catapleiite has crystallized in the presence of a free, aqueous fluid.

At constant temperature and pressure, with external buffering of TiO_2 and REE_2O_3, nine coexisting phases (e.g. microcline + albite + nepheline + biotite + clinopyroxene + pyrochlore + two zirconium silicate minerals + volatile-bearing silicate liquid) define a formally divariant mineral assemblage in the chlorine-free sub-system, which can be represented by a plane in 3D log activity space. For reactions involving eudialyte, $ClO_{-0.5}$ must be included as a component, and the number of phases present must be increased to 10, adding sodalite. The divariant planes separate (trivariant) stability volumes for the single zirconium silicate minerals, pairs of planes intersect along univariant lines (10 phases in the chlorine-free subsystem) and three planes intersect in isobaric–isothermal invariant points represented by 11 (or 12, including sodalite) coexisting phases.

A reaction between several phases and/or chemical species in a multicomponent system can be written as

$$\sum_i n_i X_i = 0$$

where n_i is the stoichiometric coefficient of the ith species involved in the reaction (X_i). By convention, n_i is positive

Table 4: Divariant mineral reactions between zirconium silicate minerals, major pegmatite minerals and melt

Fluorite saturation

(1) $0{\cdot}25\ Ne + 0{\cdot}08\ Kf + 1{\cdot}00\ Hd_{cpx} + 2{\cdot}00\ HF = 1{\cdot}00\ Flu + 0{\cdot}75\ Ab + 0{\cdot}33\ Ann_{bi} + 0{\cdot}67\ H_2O$

Sodalite–nepheline–HCl reaction

(2) $0{\cdot}38\ Ab + 0{\cdot}88\ Ne + 0{\cdot}50\ H_2O + 0{\cdot}50\ Nds + 1{\cdot}00\ HCl = 1{\cdot}00\ Sod + 0{\cdot}88\ Kf$

Hiortdahlite volume

(3) $0{\cdot}89\ Hio + 2{\cdot}60\ Ab + 1{\cdot}25\ Ann_{bi} + 0{\cdot}26\ H_2O = 1{\cdot}00\ Zrc + 0{\cdot}87\ Ne + 0{\cdot}38\ Kf + 3{\cdot}96\ Hd_{cpx} + 0{\cdot}08\ TiO_2 + 0{\cdot}05\ Pcl + 0{\cdot}04\ REE_2O_3 + 0{\cdot}78\ Nds + 3{\cdot}01\ HF$

(4) $0{\cdot}89\ Hio + 2{\cdot}60\ Ab + 1{\cdot}15\ Ann_{bi} + 2{\cdot}36\ H_2O = 1{\cdot}00\ Cat + 0{\cdot}86\ Ne + 0{\cdot}28\ Kf + 3{\cdot}66\ Hd_{cpx} + 0{\cdot}081\ TiO_2 + 0{\cdot}05\ Pcl + 0{\cdot}04\ REE_2O_3 + 0{\cdot}08\ Nds + 3{\cdot}00\ HF$

(5) $0{\cdot}87\ Hio + 0{\cdot}45\ Ab + 0{\cdot}01\ Kf + 0{\cdot}14\ Ann_{bi} + 0{\cdot}08\ TiO_2 + 0{\cdot}29\ Pcl + 0{\cdot}61\ H_2O + 0{\cdot}07\ Nds = 1{\cdot}00\ Woe + 0{\cdot}15\ Ne + 0{\cdot}41\ Hd_{cpx} + 0{\cdot}03\ REE_2O_3 + 1{\cdot}50\ HF$

(6) $0{\cdot}92\ Hio + 0{\cdot}29\ Ab + 0{\cdot}17\ Ann_{bi} + 0{\cdot}58\ TiO_2 + 0{\cdot}02\ REE_2O_3 + 0{\cdot}36\ Nds = 1{\cdot}00\ Ros + 0{\cdot}10\ Ne + 0{\cdot}08\ Kf + 0{\cdot}58\ Hd_{cpx} + 0{\cdot}01\ Pcl + 0{\cdot}13\ HF + 0{\cdot}11\ H_2O$

Wöhlerite volume

(7) $1{\cdot}02\ Woe + 2{\cdot}14\ Ab + 1{\cdot}10\ Bi = 1{\cdot}00\ Zrc + 0{\cdot}71\ Ne + 0{\cdot}39\ Kf + 3{\cdot}54\ Hd_{cpx} + 0{\cdot}17\ TiO_2 + 0{\cdot}35\ Pcl + 0{\cdot}01\ REE_2O_3 + 0{\cdot}85\ Nds + 0{\cdot}44\ H_2O + 1{\cdot}48\ HF$

(8) $1{\cdot}02\ Woe + 2{\cdot}14\ Ab + 1{\cdot}00\ Ann_{bi} + 1{\cdot}66\ H_2O = 1{\cdot}00\ Cat + 0{\cdot}71\ Ne + 0{\cdot}29\ Kf + 3{\cdot}24\ Hd_{cpx} + 0{\cdot}17\ TiO_2 + 0{\cdot}35\ Pcl + 0{\cdot}01\ REE_2O_3 + 0{\cdot}15\ Nds + 1{\cdot}48\ HF$

(9) $1{\cdot}05\ Woe + 0{\cdot}06\ Ne + 0{\cdot}02\ Ann_{bi} + 0{\cdot}49\ TiO_2 + 0{\cdot}05\ REE_2O_3 + 0{\cdot}29\ Nds + 1{\cdot}45\ HF = 1{\cdot}00\ Ros + 0{\cdot}19\ Ab + 0{\cdot}09\ Kf + 0{\cdot}15\ Hd_{cpx} + 0{\cdot}32\ Pcl + 0.\ 83\ H_2O$

Zircon–catapleiite

(10) $1{\cdot}00\ Zrc + 0{\cdot}10\ Kf + 0{\cdot}30\ Hd_{cpx} + 2{\cdot}10\ H_2O + 0{\cdot}70\ Nds = 1{\cdot}00\ Cat + 0{\cdot}10\ Ann_{bi}$

Eudialyte volume

(11) $0{\cdot}32\ Eud + 0{\cdot}63\ Ne + 0{\cdot}06\ Kf + 1{\cdot}33\ Hd_{cpx} + 0{\cdot}15\ TiO_2 + 0{\cdot}27\ Pcl + 1{\cdot}45\ HF = 1{\cdot}00\ Woe + 1{\cdot}85\ Ab + 0{\cdot}75\ Ann_{bi} + 0{\cdot}08\ REE_2O_3 + 0{\cdot}13\ H_2O + 0{\cdot}84\ Nds + 0{\cdot}35\ Sod$

(12) $0{\cdot}37\ Eud + 0{\cdot}90\ Ne + 0{\cdot}05\ Kf + 1{\cdot}99\ Hd_{cpx} + 0{\cdot}07\ TiO_2 + 3{\cdot}39\ HF = 1{\cdot}00\ Hio + 2{\cdot}49\ Ab + 1{\cdot}02\ Ann_{bi} + 0{\cdot}02\ Pcl + 0{\cdot}06\ REE_2O_3 + 0{\cdot}84\ H_2O + 1{\cdot}04\ Nds + 0{\cdot}40\ Sod$

(13) $0{\cdot}34\ Eud + 0{\cdot}73\ Ne + 1{\cdot}25\ Hd_{cpx} + 0{\cdot}64\ TiO_2 + 2{\cdot}98\ HF = 1{\cdot}00\ Ros + 2{\cdot}14\ Ab + 0{\cdot}03\ Kf + 0{\cdot}77\ Ann_{bi} + 0{\cdot}03\ Pcl + 0{\cdot}04\ REE_2O_3 + 0{\cdot}59\ H_2O + 0{\cdot}41\ Nds + 0{\cdot}37\ Sod$

(14) $0{\cdot}33\ Eud + 0{\cdot}25\ Ab + 0{\cdot}24\ Ann_{bi} + 1{\cdot}61\ H_2O + 0{\cdot}01\ HF = 1{\cdot}00\ Cat + 0{\cdot}07\ Ne + 0{\cdot}23\ Kf + 1{\cdot}89\ Hd_{cpx} + 0{\cdot}07\ Pcl + 0{\cdot}02\ TiO_2 + 0{\cdot}09\ REE_2O_3 + 1{\cdot}00\ Nds + 0{\cdot}35\ Sod$

(15) $0{\cdot}33\ Eud + 0{\cdot}38\ Ab + 0{\cdot}24\ Ne + 0{\cdot}35\ Ann_{bi} = 1{\cdot}00\ Zrc + 0{\cdot}66\ Kf + 2{\cdot}19\ Hd_{cpx} + 0{\cdot}02\ TiO_2 + 0{\cdot}07\ Pcl + 0{\cdot}10\ REE_2O_3 + 0{\cdot}68\ H_2O + 1{\cdot}52\ Nds + 0{\cdot}36\ Sod$

Låvenite volume

(16) $0{\cdot}60\ Lav + 0{\cdot}40\ Ne + 0{\cdot}50\ Kf + 2{\cdot}44\ Hd_{cpx} + 0{\cdot}27\ Pcl + 0{\cdot}01\ REE_2O_3 + 0{\cdot}91\ H_2O = 1{\cdot}00\ Woe + 1{\cdot}20\ Ab + 0{\cdot}89\ Ann_{bi} + 0{\cdot}01\ TiO_2 + 0{\cdot}03\ Nds + 0{\cdot}05\ HF$

(17) $0{\cdot}61\ Lav + 0{\cdot}91\ Ab + 0{\cdot}12\ Kf + 0.\ 19\ Ann_{bi} + 0{\cdot}58\ H_2O = 1{\cdot}00\ Zrc + 0{\cdot}30\ Ne + 1{\cdot}05\ Hd_{cpx} + 0{\cdot}18\ TiO_2 + 0{\cdot}07\ Pcl + 0{\cdot}01\ REE_2O_3 + 0{\cdot}88\ Nds + 1{\cdot}53\ HF$

(18) $0{\cdot}69\ Lav + 0{\cdot}63\ Ne + 0{\cdot}58\ Kf + 3{\cdot}28\ Hd_{cpx} + 0{\cdot}04\ REE_2O_3 + 0{\cdot}36\ H_2O + 1{\cdot}66\ HF = 1{\cdot}00\ Hio + 1{\cdot}90\ Ab + 1{\cdot}19\ Ann_{bi} + 0{\cdot}02\ Pcl + 0{\cdot}11\ TiO_2 + 0{\cdot}12\ Nds$

(19) $1{\cdot}86\ Lav + 2{\cdot}02\ Ab + 137\ Kf + 3{\cdot}49\ Hd_{cpx} + 0{\cdot}28\ REE_2O_3 + 3{\cdot}26\ H_2O + 2{\cdot}51\ Nds + 1{\cdot}09\ HCl = 1{\cdot}00\ Eud + 0{\cdot}71\ Ne + 0{\cdot}46\ Ann_{bi} + 0{\cdot}49\ TiO_2 + 4{\cdot}70\ HF$

Rosenbuschite–catapleiite

(20) $0{\cdot}97\ Ros + 2{\cdot}23\ Ab + 0{\cdot}98\ Ann_{bi} + 2{\cdot}46\ H_2O = 1{\cdot}00\ Cat + 0{\cdot}77\ Ne + 0{\cdot}21\ Kf + 3{\cdot}10\ Hd_{cpx} + 0{\cdot}04\ Pcl + 0{\cdot}64\ TiO_2 + 0{\cdot}06\ REE_2O_3 + 0{\cdot}43\ Nds + 2{\cdot}88\ HF$

Abbreviations used for idealized endmember minerals and dissolved components in the melt are given in Table 3.

for products and negative for reactants. The equilibrium constant for the reaction ($\log K$) is given by

$$\log K = \sum_i n_i \log a_i$$

where a_i is the activity of the ith species.

In the present case, the reactants and products are: (1) solid phases of constant composition (endmember feldspar, nepheline, sodalite, hydroxy-annite, zirconium silicate minerals); (2) endmembers in multicomponent solid solutions (the $CaFeSi_2O_6$ component in aegirine–augite, $NaCaNb_2O_6F$ in pyrochlore); (3) externally buffered, minor oxides (TiO_2, REE_2O_3); (4) the three species of interest, *Nds*, H_2O and HF. Assuming that the activities of the pure solids are unity, the equation can then be rewritten

$$\log K = \left(\sum n_i \log a_i\right)_{\text{solid solutions}} + \left(\sum n_j \log a_j\right)_{\text{externally buffered components}} + n_{Nds} \log a_{Nds} + n_{H_2O} \log a_{H_2O} + n_{HF} \log a_{HF}.$$

Only the three last terms include the activities of $Na_2Si_2O_5$, H_2O and HF in the pegmatite magma. In the absence of thermodynamic data on the participating minerals and oxide species in the silicate liquid, ΔG for the reaction, and thereby $\log K$, cannot be determined. Furthermore, the activity terms for the pyrochlore and clinopyroxene solid solution, and for the minor oxide species are (at best) poorly constrained. Nevertheless, all these terms can be regarded as constant with respect to the three activity terms of interest, and the equation simplifies to

$$n_{Nds} \log a_{Nds} + n_{H_2O} \log a_{H_2O} + n_{HF} \log a_{HF} = \text{constant}.$$

This is the equation of a plane in an orthogonal, 3D coordinate system with $\log a_{Nds}$, $\log a_{H_2O}$ and $\log a_{HF}$ as axes. Although the right-hand side of the equation (and hence the absolute coordinates of the plane) remains unconstrained, its orientation in activity space is uniquely given by the ratios of the stoichiometric coefficients; for example, the slope of the intersection of a plane with a section parallel with the $\log a_{Nds}$ and $\log a_{HF}$ axes is given by $-n_{Nds}/n_{HF}$, and similar for the slopes in the projections defined by the two other combinations of orthogonal axes.

An internally consistent petrogenetic grid

Using idealized phase compositions listed in Table 3, 20 formally divariant, balanced mineral–melt reactions can be defined (Table 4).

Fluorite-saturated case

For the fluorite-saturated case comparison with observed mineral assemblages is necessary to determine which of several possible configurations of divariant reactions in 3D activity space represent the phase equilibria appropriate for the nepheline syenite pegmatites. Although both the fluorite-saturated and -undersaturated domains must be considered, it is most convenient to start with the distribution of stability fields at fluorite saturation, as this reduces the problem to a case of 2D Schreinemakers analysis. Figure 5a shows five possible configurations of stability fields in the fluorite-saturated, Cl-free subsystem surrounding the hiortdahlite (*Hio*) field (shaded) in a projection onto the $\log a_{Nds}$–$\log a_{H_2O}$ plane. Mineral assemblages that are forbidden in scenarios *iii*, *iv* and *v* have been found to exist in the pegmatites (*Flu* + *Zrc* + *Cat*, *Flu* + *Zrc* + *Hio*, *Flu* + *Hio* + *Cat*, *Flu* + *Hio* + *Ros*, *Lav* + *Flu*), whereas observed mineral assemblages agree with the predictions of scenarios *i* and *ii* (Fig. 5b). If wöhlerite does not coexist in equilibrium with fluorite, the four-phase assemblage *Hio* + *Cat* + *Ros* + *Flu* is stable (scenario *i* in Fig. 5). If, on the other hand, wöhlerite is stable with fluorite, this assemblage would be replaced by three four-phase assemblages involving fluorite with wöhlerite and two of the minerals hiortdahlite, catapleiite and rosenbuschite (scenario *ii* in Fig. 5). None of the critical four-phase assemblages that would confirm the validity of either scenario *i* or *ii* have been observed. Although the present observations do not support the existence of any magmatic mineral assemblage involving stable *Woe* + *Flu*, there is no conclusive evidence against. We therefore chose scenario *ii* as the preferred alternative, but with a *Woe* + *Flu* field that is small, and/or restricted to combinations of H_2O and Nds activities that are not realized in the nepheline syenite pegmatites. It is possible that other geometrical configurations will be stabilized by changes in temperature, pressure or other parameters not considered here. For example, decreasing f_{O2} would be likely to expand the stability field of låvenite with essential Fe^{2+} at the expense of the low-iron zirconium silicate minerals, eventually stabilizing a configuration like scenario *iv* in Fig. 5a.

The 3D petrogenetic grid

The 2D configuration of the fluorite saturation plane (Fig. 5a) constrains the geometry of the fluorite-undersaturated part of the 3D petrogenetic grid. The divariant fluorite saturation surface (reaction (1) in Table 4) is parallel to the $\log a_{Nds}$ axis, and has a positive slope of 0·33 in the $\log a_{H_2O}$–$\log a_{HF}$ projection (Fig. 6). The stability field boundaries in Fig. 5 are the intersections of this plane with divariant surfaces in the fluorite-undersaturated system, the features of which are conveniently illustrated in a projection of the fluorite saturation surface to the $\log a_{Nds}$–$\log a_{H_2O}$ plane (Fig. 7a) and in sections parallel to the $\log a_{Nds}$–$\log a_{HF}$ and $\log a_{H_2O}$–$\log a_{HF}$ planes (Fig. 7b–g). The grid is semiquantitative, in the sense that it is internally consistent and gives a true representation of the relative slopes of the divariant

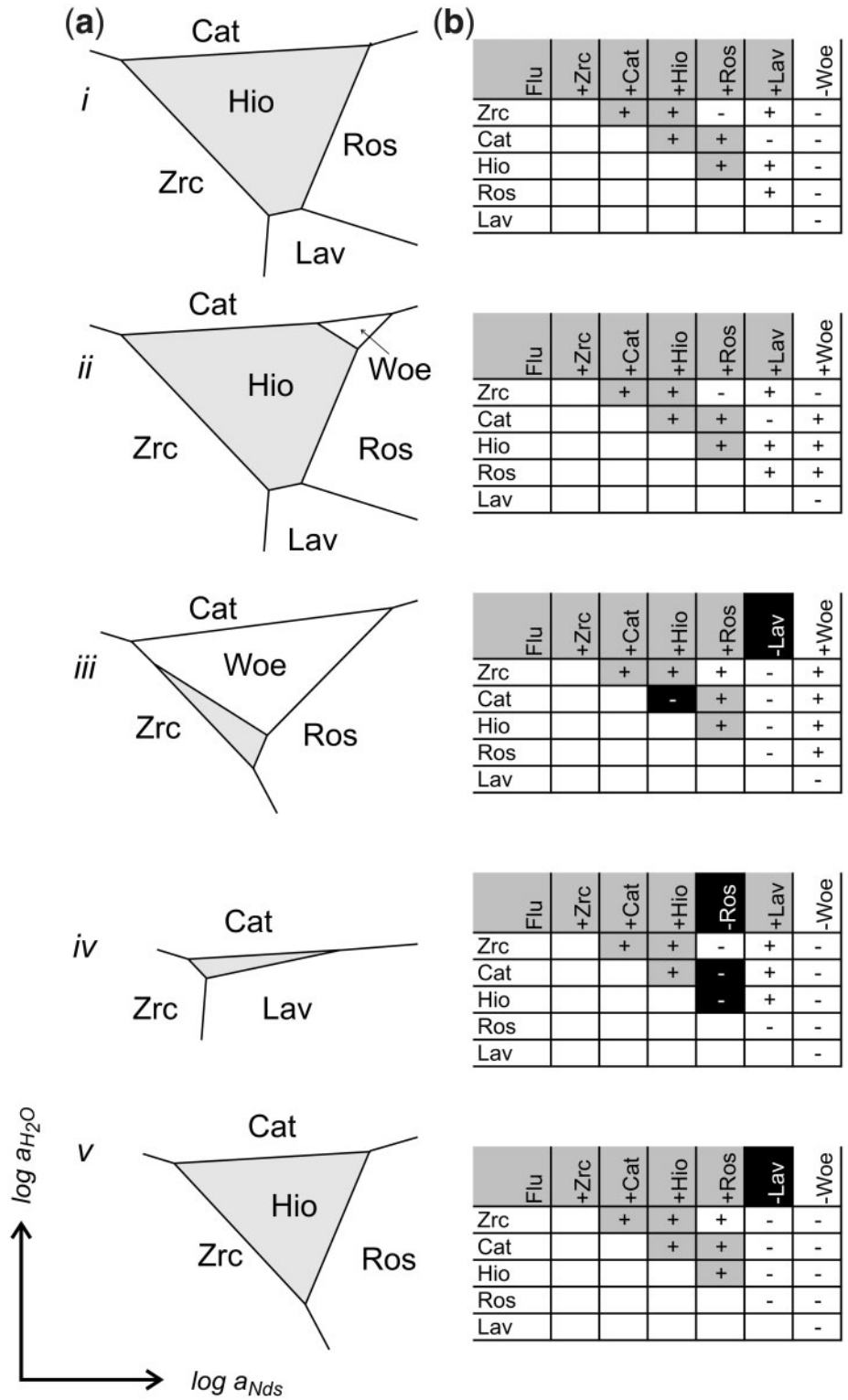

Fig. 5. (a) Possible configurations of stability fields of hiortdahlite (*Hio*, shaded), zircon (*Zrc*), catapleiite (*Cat*), rosenbuschite (*Ros*), låvenite (*Lav*) and wöhlerite (*Woe*) in the presence of fluorite, projected to the log a_{Nds}–log a_{H_2O} plane (*Nds* is the $Na_2Si_2O_5$ component in the pegmatite melt). Scenarios *i*–*v* show five mutually exclusive configurations of stability fields, which are all consistent with a 3D Schreinemakers analysis of the divariant reactions in Table 4 in log a_{Nds}–log a_{H_2O}–log a_{HF} space. (b) Two- and three-phase assemblages predicted from the geometrical configurations in (a). For each matrix, the header row shows single phases expected to be stable (+) or unstable (−) with fluorite. In the body of the matrix, pairs of phases that are expected to occur stably with fluorite are indicated by (+), and combinations that are not expected to occur by (−). Grey shades represent predicted phase assemblages that have actually been observed in the pegmatites, and black fields 'forbidden' combinations that have been found in the samples. Observation of one or more 'forbidden' phase assemblages is evidence against that particular stability field configuration.

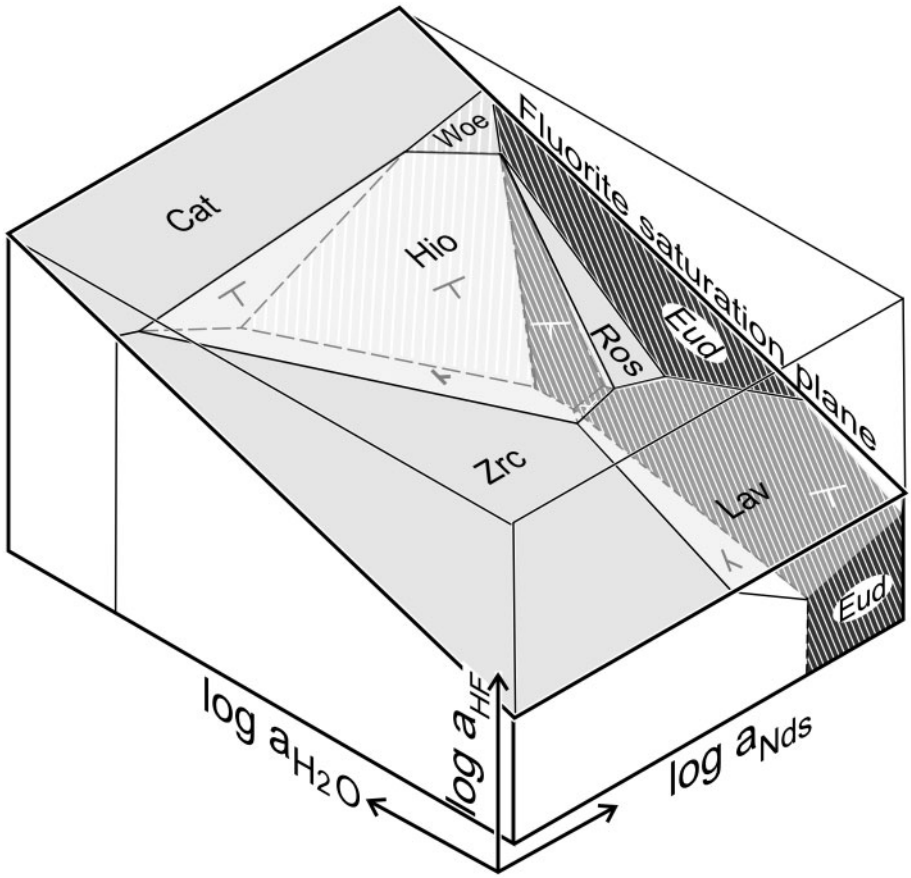

Fig. 6. A 3D view of the petrogenetic grid in log a_{Nds}–log a_{H_2O}–log a_{HF} space showing the phase stability fields at, and immediately below, the fluorite saturation surface. The 3D stability volume of wöhlerite (Woe), shown in grey and white stripes, has for illustration been drawn to intersect the fluorite saturation surface (i.e. scenario *ii* in Fig. 5), although evidence for the stability of a Woe + Flu assemblage is lacking (see discussion in the text). The hiortdahlite and låvenite fields have been left semi-transparent, to expose the fluorite-absent stability fields involving these minerals. The orientations of divariant planes below the fluorite saturation surface are indicated by strike-and-dip symbols. At fluorite saturation, the eudialyte field (dark stripes) will be separated from the zircon field by the låvenite, hiortdahlite and wöhlerite fields, which wedge out towards lower a_{Hf}; this will allow Eud + Zrc assemblages at a_{Hf} well below fluorite saturation, but not a stable Eud + Zrc + Flu assemblage.

planes and univariant lines in 3D log activity space, and of the relative positions of the stability volumes of the single zirconium silicate minerals. However, it gives no information on the absolute values of component activities, and the relative sizes of the divariant fields and the stability volumes of single phases are arbitrary. Quantitative calibration of the grid would require experimental data on critical mineral assemblages, and/or thermodynamic data on the zirconium silicate minerals and on components in the volatile-bearing silicate melt, none of which is available.

The chlorine-free subsystem has stability volumes for catapleiite, zircon, wöhlerite, hiortdahlite, rosenbuschite and låvenite. The boundary between the zircon and catapleiite volumes is subparallel to the log a_{HF} axis, and at very low a_{HF}, these two, and the stability volume of eudialyte are the only ones that need to be considered (Fig. 7b and c). The wedge-shaped stability volumes for wöhlerite, låvenite and rosenbuschite occur at higher a_{HF} levels, and expand towards increasing a_{Nds}, but are truncated by the eudialyte volume at elevated HCl activity. The stability volume of hiortdahlite is bounded by the volumes of zircon (at low a_{Nds}), catapleiite (high a_{H_2O}), rosenbuschite (high a_{Nds}), wöhlerite (low a_{HF}), låvenite (low a_{H_2O}) and eudialyte (high a_{Nds} and a_{HCl}). The relative slopes of the divariant planes limiting the hiortdahlite volume are such that the volume can never extend to great depths within the fluorite-undersaturated part of the diagram. Hiortdahlite is therefore stable in nepheline syenite magmas only at or close to saturation with fluorite. The same can be said about rosenbuschite, but in low-Cl systems, the rosenbuschite volume and the *Ros* + *Woe* plane will extend to increasingly greater depths below fluorite saturation at increasing a_{Nds}.

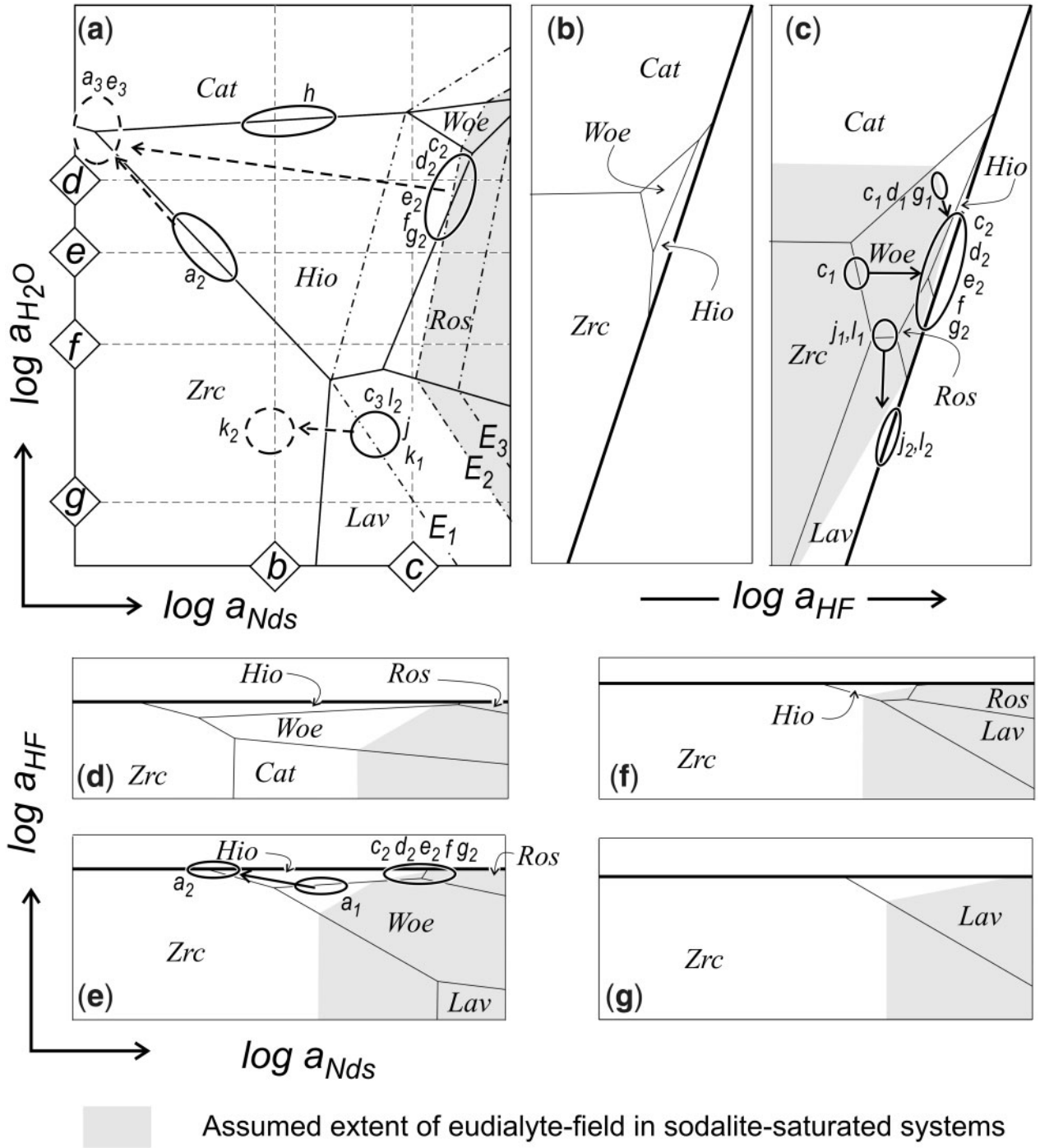

Fig. 7. Sections through the semiquantitative, 3D petrogenetic grid in the multicomponent system in log a_{Nds}–log a_{H_2O}–log a_{HF} space, drawn according to scenario *ii* in Fig. 5. *Zrc*, zircon; *Cat*, catapleiite; *Ros*, rosenbuschite; *Lav*, låvenite; *Hio*, hiortdahlite; *Woe*, wöhlerite. Inferred crystallization conditions for the pegmatites in this study are shown as circles and ellipses. Inferred evolution with time is indicated by arrows. Continuous-line outlines and arrows reflect conditions during magmatic crystallization, dashed-line outlines and arrows post-magmatic, fluid-induced reactions. The circled fields are linked to the corresponding mineral assemblages in Table 2 by lower-case letters. (a) The fluorite saturation surface (Fig. 6), projected to the log a_{Nds}–log a_{H_2O} plane. Thin dashed lines identified by letters enclosed in diamonds give the positions of the sections shown in Fig. 7b–g. The extent of the eudialyte field is unconstrained; its maximum possible size is given by dash–dot line E_1, which touches at the *Flu* + *Zrc* + *Hio* + *Lav* point. The shaded field limited by dash–dot line E_2 is a more realistic field for *Eud* + *Flu* in the presence of *Ne* + *Sod*, as it allows observed assemblages involving fluorite, hiortdahlite, rosenbuschite and wöhlerite within a restricted range of component activities, as illustrated by assemblages c_2, d_2, e_2, f and g_2. At sodalite-undersaturated conditions, the eudialyte field is shifted to higher a_{Nds} (dash–dot line E_3). (b, c) log a_{HF}–log a_{H_2O} sections through the 3D petrogenetic grid along profiles indicated in (a). The bold line represents the fluorite saturation surface (i.e. the maximum possible a_{HF} in this system). The shaded field is the assumed extent of the eudialyte field in the presence of nepheline and sodalite. (d–g) log a_{Nds}–log a_{HF} sections, as indicated in (a).

The HCl activity is not tied to the other components by mixed volatile reactions. The maximum a_{HCl} is limited by the simultaneous crystallization of nepheline and sodalite (reaction (2) in Table 4). In the Cl-bearing system, a volume for eudialyte will appear at high a_{Nds}, and expand towards lower a_{Nds} with increasing a_{HCl}. The non-existence of a stable *Zrc* + *Eud* + *Flu* assemblage indicates that the eudialyte field does not extend as far into the diagram as the *Zrc* + *Lav* + *Hio* + *Flu* point; the dash–dot line E_1 in Fig. 7a therefore represents an absolute maximum for the stability field of eudialyte in these pegmatites. However, the existence of assemblages with rosenbuschite + fluorite indicates that the real eudialyte stability field is significantly smaller, as suggested by lines E_2 and E_3. We tentatively assume that E_2 represents the real maximum extent of the eudialyte field (i.e. in a system with nepheline + sodalite), as it will allow the observed mineral assemblages with wöhlerite, rosenbuschite, hiortdahlite ± eudialyte within a relatively small range of component activities. The predicted four-phase assemblage *Hio* + *Ros* + *Eud* + *Flu* has been observed in the present samples (Table 2). On the other hand, none of the three- and four phase assemblages involving both låvenite and hiortdahlite have been observed, indicating that the *Lav* + *Hio* + *Flu* univariant in Fig. 6 and 7a represents a minimum limit for the water activity at the magmatic stage of crystallization of the hiortdahlite-bearing pegmatites. On the other hand, primary coexistence of låvenite and fluorite without hiortdahlite has been observed in the samples from Låven island, suggesting that the water activity was low at least in parts of that pegmatite.

DISCUSSION

Contrasting crystallization conditions in Oslo Rift nepheline syenite pegmatites

The different liquidus mineral assemblages recorded in the nepheline syenite pegmatites reflect differences in water and hydrogen fluoride activity and alkali enrichment of the magma (Fig. 7). In the Langodden pegmatite, the inclusion assemblage with wöhlerite + hiortdahlite (a_1) indicates an early stage of crystallization at fluorite-undersaturated conditions. The following stages of evolution with coexisting hiortdahlite + zircon + fluorite (a_2) and zircon + catapleiite + fluorite (a_3) reflect crystallization at higher a_{HF} and lower a_{Nds}, followed by an increase in a_{H_2O}. This relative decrease of alkalinity and increase of water has not been seen in other pegmatites examined in this study.

In the Stokksund pegmatite, the hiortdahlite + fluorite + catapleiite mineralogy (assemblage *h* in Table 2 and Fig. 7a) reflects magmatic crystallization at elevated a_{H_2O} and a_{HF}, as fluorite saturation in the presence of hiortdahlite and catapleiite requires higher a_{HF} than any of the other hiortdahlite-bearing mineral assemblages observed.

The evolution from wöhlerite-bearing assemblages (assemblages c_1, d_1, g_1) to hiortdahlite + rosenbuschite ± eudialyte (c_2, d_2, g_2) in the pegmatites from Trompetholmen, Risøya and Skutesundskjær suggests a trend at increasing activities of HF and Nds, ending up at the *Hio* + *Ros* + *Eud* + *Flu* point, which may be the high-alkali endpoint for any nepheline syenite magma crystallizing hiortdahlite. The Arøyskjærene pegmatite also has the *Hio* + *Ros* + *Eud* + *Flu* assemblage (e_2), but lacks evidence of the early, crystallization stage at lower a_{HF}.

In the Låven pegmatite, an early stage of wöhlerite + låvenite (l_1) crystallization is followed by låvenite + fluorite (l_2), combined with alteration of wöhlerite to low-iron låvenite. Hiortdahlite has not been reported from this pegmatite, so, although the låvenite + fluorite assemblage suggests crystallization at lower a_{H_2O} than in any of the other pegmatites studied, the relationship to the *Hio* + *Lav* + *Flu* line in Fig. 7 cannot be determined. A trend towards low water activity could be caused by local crystallization of a hydroxy-annite or other water-bearing major minerals. The Låven pegmatite has a complex mineralogy and an uneven distribution of mineral assemblages (Brøgger, 1890; Liestøl, 1956; Larsen, 2006, 2010). The presence of catapleiite-bearing mineral assemblages at Låven is very well documented, as the island is the type locality for catapleiite (Weibye, 1850). Together, these observations suggest that this pegmatite had a heterogeneous distribution of volatile activities or a fluid regime that changed with time, or a combination of the two.

Whereas these findings show diversity of volatile activity in the pegmatites, there is also a clear tendency of clustering around the intersection of the eudialyte field with the hiortdahlite, rosenbuschite and wöhlerite fields, and a change from fluorite-undersaturated liquidus assemblages with wöhlerite to fluorite-saturated assemblages (Fig. 7a and c). This is most probably due to enrichment of fluorine in the residual melt caused by growth of fluorine-free minerals (feldspar, nepheline, clinopyroxene) from a fluorine-bearing, but initially fluorite-undersaturated melt. Increasing residual fluorine led to the stabilization of wöhlerite-bearing assemblages, and finally to fluorite-saturated assemblages with hiortdahlite, rosenbuschite or låvenite (Fig. 7c). The post-magmatic evolution in the pegmatites has in common a strong decrease in a_{Nds}, and increase in water.

The effect of oxygen fugacity on zirconium silicate mineral assemblages

Although oxygen fugacity has not been included in the model calculations, some inferences on the effect of changes in f_{O2} can be made. Magnetite and biotite are common

minerals in the pegmatites, and f_{O2} is likely to be controlled by the reaction

$$Ann_{bi} + 0{\cdot}5O_2 = Mag + Kf + H_2O$$

where *Mag* is the Fe_3O_4 component in titanomagnetite. This is not a formally univariant oxygen buffer curve, as it depends on mineral compositions and water activity, but as long as biotite and titanomagnetite remain stable, it will prevent wide excursions in oxygen fugacity level. This suggests that the pegmatites have crystallized at mildly reducing conditions around QFM − 1, corresponding to those of the host larvikite (Neumann, 1976).

As long as the major liquidus mineralogy of the pegmatite magma remains unchanged, the relative stability relationships of the iron-poor Zr-silicate minerals are likely to be little affected. The exception may be låvenite, which has essential Fe^{2+} and Mn^{2+}. At increasing oxygen fugacity, the låvenite stability field will decrease, and låvenite will be replaced by zircon + magnetite ± fluorite symplectites (Fig. 2k). Increasing oxygen fugacity would also be expected to increase the stability fields of hiortdahlite and rosenbuschite to lower water activity, at the expense of låvenite. (Fig. 6). Oxidation of låvenite took place at a late magmatic to hydrothermal stage in the pegmatites, but at the magmatic stage, the opposite relationship is observed: hiortdahlite and wöhlerite were replaced by low-iron låvenite, and eudialyte by low-iron låvenite-bearing symplectite. This suggests an overall decreasing trend in oxygen fugacity towards the final stages of magmatic crystallization in the pegmatites.

Petrological implications

The factors controlling the change from a miaskitic crystallization regime with zircon to one with agpaitic zirconium silicate assemblages can be illustrated by a constant a_{HF} section through log a_{Nds}–log a_{H_2O}–log a_{Hf} space at low HF activity, below the point of coexisting wöhlerite, catapleiite, zircon and eudialyte in Fig. 7b (Fig. 8). A peralkaline nepheline syenite magma crystallizing within the primary field of zircon may change to a liquidus assemblage with eudialyte at increasing a_{Nds}, in agreement with the traditional view of the miaskitic to agpaitic transition in peralkaline nepheline syenites (e.g. Larsen & Sørensen, 1987). In contrast, the presence of primary catapleiite indicates elevated water activity, rather than elevated sodium silicate activity. It should be noted, however, that the shift from zircon- to catapleiite-dominated liquidus mineralogies is possible only in highly alkaline systems; at lower alkali activities, water saturation may be reached before catapleiite can form. Within the white part of the zircon primary field in Fig. 8, a magma will remain miaskitic at increasing a_{HF}, and the distinctive mineral assemblages will be zircon followed by zircon + fluorite.

The most interesting behaviour is seen within the transitional zone within the zircon primary field at low a_{HF} in Fig. 7. Within this area, the liquidus zirconium silicate mineral assemblage of a nepheline syenite magma can be forced to change from miaskitic with stable zircon, to 'low agpaitic' assemblages with different successions of wöhlerite-, hiortdahlite- and låvenite-bearing assemblages by a simple increase in a_{HF} without simultaneous changes in either water or alkali activity.

This suggests that there are at least three liquid lines of descent leading from a miaskitic to an agpaitic crystallization regime in peralkaline nepheline syenite magmas: (1) the classical case of increasing peralkalinity, leading to eudialyte-dominated mineral assemblages, and from there, possibly, to hyperagpaitic residual liquids (e.g. Andersen & Sørensen, 2005); (2) the increasing water path, leading to the stabilization of catapleiite-bearing liquidus assemblages without eudialyte, and possibly, to saturation with an aqueous fluid phase; (3) the increasing fluorine trend, leading to hiortdahlite-, låvenite- and wöhlerite-dominated mineral assemblages, and eventually to crystallization of magmatic fluorite. Increasing fluorine concentration in the melt may cause the degree of polymerization of the magma to decrease (Mysen & Virgo, 1985).

For transitionally agpaitic magmas forming the Oslo Rift pegmatites, the combination of a relatively low a_{Nds} in the parent magma and the elevated fluorine content leading to the stabilization of magmatic fluorite causes a barrier against evolution towards the more extreme compositions seen in highly agpaitic rocks such as the lujavrites of the Ilímaussaq intrusion. The alkali enrichment of a magma crystallizing a low-Na assemblage with hiortdahlite + fluorite will terminate at the *Ros* + *Hio* + *Flu* or *Eud* + *Hio* + *Flu* field boundaries, and the four-phase assemblage *Ros* + *Eud* + *Hio* + *Flu* may represent the highest attainable a_{Nds} in a such a fluorite-saturated system. Further evolution to the extreme alkali enrichment permitting crystallization of mineral assemblages with villiaumite, ussingite and other minerals typical of hyperagpaitic rocks (Khomyakov, 1995; Sørensen, 1997) is impossible or at least highly unlikely in such a magma.

Separation and loss of an aqueous fluid would deplete the system in soluble components, mainly Na, K and Cl, but also to some extent F, as shown by the existence of late, crosscutting fluorite veins in many of the pegmatites. Loss of such a fluid can explain the formation of less alkaline secondary assemblages in some of the pegmatites (e.g. assemblages d_3 at Risøya, k_2 at Låven). On the other hand, interaction between an alkali-chloride enriched, mobile fluid phase and less alkaline rocks could lead to the formation of metasomatic agpaitic mineral assemblages in otherwise miaskitic rocks, as has been observed in, for example, Tamazeght (e.g. Schilling *et al.*, 2009).

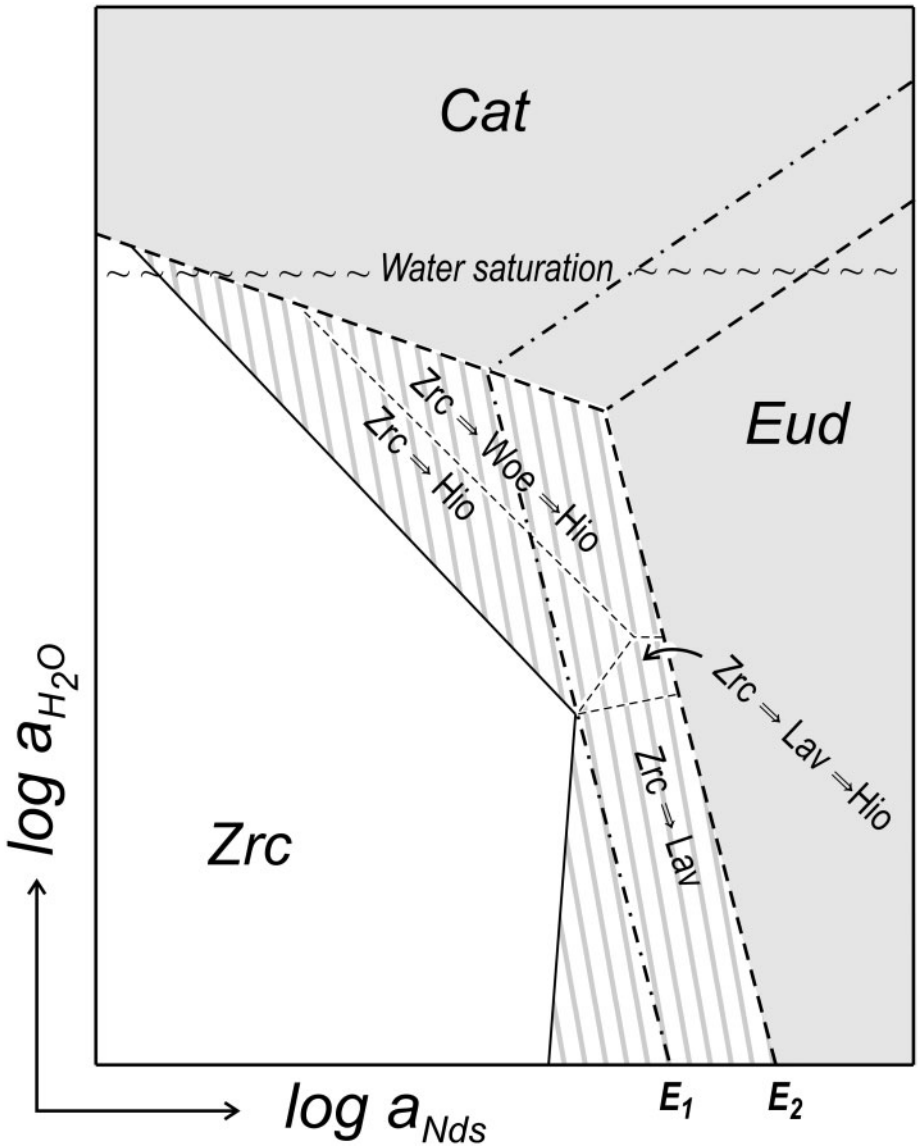

Fig. 8. A section through 3D log a_{Nds}–log a_{H_2O}–log a_{HF} space at constant a_{HF} well below the point of *Woe* + *Cat* + *Zrc* + *Eud* coexistence in Fig. 7 showing the 'agpaitic' (grey), 'transitional' (ruled) and 'miaskitic' (white) fields of crystallization in peralkaline nepheline syenite systems. Lines E_1 and E_2 are 'absolute' and 'realistic' maximum limits for the eudialyte field, taken from Fig. 7a. In the miaskitic field, zircon remains stable at any a_{HF}. Eudialyte is stable only at elevated a_{Nds}, and an increase in the peralkalinity of the system is needed to stabilize it at the expense of zircon or catapleiite at any level of a_{HF}. Within the transitional field, a magma crystallizing zircon at low a_{HF} can change to transitionally agpaitic phase assemblages with hiortdahlite, wöhlerite or låvenite by a simple increase in a_{HF} without a concomitant increase in peralkalinity. Likewise, within large parts of the miaskitic and 'transitional' fields at low a_{HF}, the phase assemblage can change to a nominally agpaitic assemblage with catapleiite as the characteristic zirconium mineral by an increase in water activity with or without increasing peralkalinity. An approximate limit for water saturation is drawn to allow a free, aqueous fluid phase to develop within the stability field of catapleiite, agreeing with the observation of abundant fluid inclusions in this mineral. This boundary will intersect the *Cat* + *Zrc* plane at low a_{Nds}, preventing the stabilization of catapleiite as a liquidus mineral in less peralkaline magmas.

Metasomatic eudialyte has not been observed in any of the present samples, but crosscutting catapleiite microveins in the TYHIO sample (Fig. 2c, i.e. assemblage a_3) may have a similar origin.

Hydrocarbon-bearing fluids have formed during crystallization of large, agpaitic intrusions such as Ilímaussaq and Khibina (Konnerup-Madsen, 200l; Ryabchikov & Kogarko, 2009, and references therein). The presence of such fluids is a consequence of the low oxygen fugacity and low solidus temperature of these magmatic systems (Ryabchikov & Kogargo, 2009), rather than a controlling factor for the stability of zirconium silicate mineral

stability. Whether or not organic fluids were present in the nepheline syenite pegmatites of the Larvik Plutonic Complex is not known.

Wider implications

In the absence of thermodynamic data for the species involved in phase equilibria, the method developed here is semiquantitative. Its main importance is that differences and trends in peralkalinity and volatile activities in a crystallizing nepheline syenite magma can be detected from relatively simple identification of the liquidus mineral assemblages. The stability diagram in Figs 6 and 7 has been developed for one specific suite of mildly agpaitic rocks, characterized by high Zr/Ti silicates of the wöhlerite, eudialyte and rosenbuschite groups, which has formed at mildly reducing conditions controlled by magnetite–biotite–potassium feldspar equilibria. Except for eudialyte *s.l.*, the zirconium silicate minerals show restricted compositional variation. The results of this study may therefore be applied directly to other examples where these minerals occur in rocks with the same major mineralogy (i.e. microcline + albite + nepheline + aegirine–augite + biotite + titanomagnetite ± sodalite ± fluorite). The underlying principle (i.e. chemographic analysis based on observed assemblages of coexisting minerals and mineral compositions determined by electron microprobe) is universally applicable. Within the field of agpaitic rocks, the method may be used to identify factors controlling the relative stability of high-Ti assemblages with mosandrite, lorenzenite, rinkite, astrophyllite and other minerals that are reasonably common in agpaitic rocks, and to evaluate the parameters controlling the transition into the hyperagpaitic realm; for example, in the lujavrites of Ilímaussaq. Other chemical variables may be introduced for rocks where they are relevant (e.g. CaO for high-Ca agpaitic rocks), as may oxygen fugacity, provided the analysis is properly supported by observed mineral assemblages.

CONCLUSIONS

In the nepheline syenite pegmatites associated with larvikite and nepheline syenite in the Larvik Plutonic Complex in the Oslo Rift, Na–Ca–Zr–F silicate minerals of the wöhlerite and rosenbuschite groups form part of the liquidus mineral assemblage of highly evolved, peralkaline and volatile-enriched nepheline syenite magmas, together with the major rock-forming minerals (feldspar, alkali-rich pyroxene and amphibole, biotite, nepheline, sodalite), fluorite and eudialyte *s.l.* Because the structures of the wöhlerite- and rosenbuschite-group minerals allow only restricted compositional variation within single species, minor changes in magma composition or volatile activities may lead to stabilization of distinct zirconium silicate mineral assemblages, which are sensitive indicators of concentration-dependent parameters in these highly evolved magmas.

There are at least three types of process that may change the liquidus assemblage of a nepheline syenite magma from miaskitic with zircon to agpaitic with complex zirconium silicate minerals: (1) an increase in peralkalinity, leading to crystallization of eudialyte; (2) increasing water activity (and eventually, saturation with an aqueous fluid phase), leading to the stabilization of catapleiite-bearing mineral assemblages; (3) increasing fluorine (or HF) activity, stabilizing liquidus assemblages with wöhlerite, hiortdahlite, låvenite ± fluorite.

The findings of this study confirm that the 'low agpaitic' or 'transitional' magmas forming the nepheline syenite pegmatites in the Oslo Rift represent a distinct style of magmatic evolution, in which increasing fluorine (or HF) activity is as important as an elevated (Na + K)/Al ratio for the stabilization of complex Na–Ca–Zr silicate liquidus minerals, and thus for the transition from a miaskitic to an agpaitic crystallization regime. A peralkaline nepheline syenite magma crystallizing liquidus hiortdahlite or låvenite together with fluorite may eventually also crystallize eudialyte *s.l.* if chlorine or HCl activity is sufficiently high, but it is likely to terminate at liquidus boundaries or low-variance points involving these minerals and rosenbuschite, and not to evolve further towards hyperagpaitic residual melt compositions.

ACKNOWLEDGEMENTS

Thanks are due to Hans-Jørgen Berg for help with X-ray diffraction work, and to Ulf Hålenius and Jörgen Langhof for access to the collections of the National Museum of Natural History, and for practical assistance with the study of the material in the Stockholm collection. Helpful suggestions from Henrik Friis, Per Aagaard and Marlina Elburg, and comments from editor Ron Frost and reviewers Michael Marks, Roger Mitchell and Henning Sørensen are gratefully acknowledged. Gregor Markl and Katharina Pfaff kindly provided their Excel spreadsheet for eudialyte structural formula calculation. Special thanks go to Henning Sørensen, who introduced the first author to the fascinating world of agpaitic rocks.

FUNDING

This study was supported by grants from the "Småforsk" program of the Department of Geosciences, University of Oslo to T.A. in 2008 and 2009.

SUPPLEMENTARY DATA

Supplementary data for this paper are available at *Journal of Petrology* online.

REFERENCES

Andersen, T. & Sørensen, H. (2005). Stability of naujakasite in hyperagpaitic melts and the petrology of naujakasite lujavrite in the Ilímaussaq alkaline complex, South Greenland. *Mineralogical Magazine* **69**, 125–136.

Baker, D. R., Conte, A. M., Freda, C. & Ottolini, L. (2002). The effect of halogens on Zr diffusion and zircon dissolution in hydrous metaluminous granitic melts. *Contributions to Mineralogy and Petrology* **142**, 666–678.

Bellezza, M., Merlino, S. & Perchiazzi, N. (2009). Mosandrite: Structural and crystal-chemical relationships with rinkite. *Canadian Mineralogist* **47**, 897–908.

Brøgger, W. C. (1890). Die Mineralien der Syenitpegmatitgänge der südnorwegischen Augit- und Nephelinsyenite. *Zeitschrift für Krystallographie* **16**, 1–235 +1–663.

Christiansen, C. C., Johnsen, O. & Makovicky, E. (2003). Crystal chemistry of the rosenbuschite group. *Canadian Mineralogist* **41**, 1203–1224.

Dahlgren, S. (2010). The Larvik Plutonic Complex: The larvikite and nepheline syenite plutons and their pegmatites. In: Larsen, A. O. (ed.) *The Langesundsfjord. History, Geology, Pegmatites, Minerals*. Salzhemmerdorf, Germany: Bode, pp. 26–37.

Friis, H., Balić-Žunić, T., Williams, T. & Petersen, O. V. (2010). Minerals of the låvenite group from South Greenland and Norway. *Norsk Bergverksmuseum Skrift* **43**, 35–39.

Jarosewich, E. & Boatner, L. A. (1991). Rare-earth element reference samples for electron microprobe analysis. *Geostandards Newsletter* **15**, 397–399.

Johnsen, O. & Grice, J. D. (1999). The crystal chemistry of the eudialyte group. *Canadian Mineralogist* **37**, 865–891.

Johnsen, O., Ferraris, G., Gault, R. A., Grice, J. D., Kampf, A. R. & Pekov, I. V. (2003). The nomenclature of eudialyte-group minerals. *Canadian Mineralogist* **41**, 785–794.

Keller, J., Williams, C. T. & Koberski, U. (1995). Niocalite and wöhlerite from the alkaline and carbonatite rocks at Kaiserstuhl, Germany. *Mineralogical Magazine* **59**, 561–566.

Khomyakov, A. P. (1995). *Mineralogy of Hyperagpaitic Alkaline Rocks*. Oxford: Oxford Scientific Publications, Clarendon Press, 222 p.

Kogarko, L. N. (1974). Role of volatiles. In: Sørensen, H. (ed.) *The Alkaline Rocks*. London: John Wiley, pp. 474–487.

Konnerup-Madsen, J. (2001). A review of the composition and evolution of hydrocarbon gases during solidification of the Ilímaussaq alkaline complex, South Greenland. *Geology of Greenland Survey Bulletin* **190**, 159–166.

Larsen, A. O. (1996). Rare earth minerals from the syenite pegmatites in the Oslo Region, Norway. In: Jones, A. P., Wall, F. & Williams, C. T. (eds) *Rare Earth Minerals. Chemistry, Origin and Ore Deposits*. London: Chapman & Hall, pp. 151–166.

Larsen, A. O. (1998). Identiteten til sorte glimmere i biotittserien fra syenittpegmatitter i Langesundsfjordområdet. *Bergverksmuseets Skriftserie* **14**, 5–8.

Larsen, A. O. (2001). Chemical composition of catapleiites from the syenite pegmatites in the Larvik plutonic complex, Norway. *Bergverksmuseets Skriftserie* **18**, 5–9.

Larsen, A. O. (2006). Låven, et fredet naturminne. *Bergverksmuseets Skriftserie* **33**, 37–40.

Larsen, A. O. (2010). *The Langesundsfjord. History, Geology, Pegmatites, Minerals*. Salzhemmerdorf, Germany: Bode, 239 p.

Larsen, A. O. & Raade, G. (1997). Pyroksener fra Oslofeltets syenittpegmatitter. *Bergverksmuseets Skriftserie* **12**, 16–21.

Larsen, A. O., Åsheim, A. & Gault, R. A. (2005*a*). Minerals of the eudialyte group from the Sagåsen larvikite quarry, Porsgrunn, Norway. *Bergverksmuseets Skriftserie* **30**, 58–62.

Larsen, A. O., Åsheim, A. & Gault, R. A. (2005*b*). Ferrokentbrooksite (Brøgger's xanthopite) from Skutesundskjær in the Langesundsfjord district, Norway. *Bergverksmuseets Skriftserie* **30**, 63–67.

Larsen, B. T., Olaussen, S., Sundvoll, B. & Heeremans, M. (2008). The Permo-Carboniferous Oslo Rift through six stages and 65 million years. *Episodes* **31(1)**, 52–58.

Larsen, L. M. & Sørensen, H. (1987). The Ilímaussaq intrusion—progressive crystallization and formation of layering in an agpaitic magma. In: Fitton, J. G. & Upton, B. G. J. (eds) *Alkaline Igneous Rocks. Geological Society, London, Special Publications* **30**, 473–488.

Le Maitre, R. W. (ed.) (2003). *Igneous Rocks. A Classification and Glossary of Terms*. Cambridge: Cambridge University Press, 236 p.

Liestøl, G. B. (1956). Noen petrografiske og mineralogiske undersøkelser omkring pegmatittgangene i Langesundsfjorden. MSc thesis, Hovedoppgave i mineralogi med petrografi, University of Oslo.

Mariano, A. N. & Roeder, P. L. (1989). Wöhlerite: Chemical composition, cathodoluminescence and environment of crystallization. *Canadian Mineralogist* **27**, 709–720.

Munoz, J. L. (1984). F–OH and Cl–OH exchange in micas with application to hydrothermal ore deposits. In: Bailey, S. W. (ed.) *Micas. Mineralogical Society of America, Reviews in Mineralogy* **13**, 469–491.

Murad, E. (2006). Mineralogy of aegirine from Låven island, Langesundsfjorden, southern Norway. *Norwegian Journal of Geology* **86**, 435–438.

Mysen, B. O. & Virgo, D. (1985). Structure and properties of fluorine-bearing aluminosilicate melts: the system Na_2O–Al_2O_3–SiO_2–F at 1 atm. *Contributions to Mineralogy and Petrology* **91**, 205–220.

Neumann, E.-R. (1976). Compositional relations among pyroxenes, amphiboles and other mafic phases in the Oslo Region plutonic rocks. *Lithos* **9**, 85–109.

Neumann, E.-R. (1980). Petrogenesis of the Oslo Region larvikites and associated rocks. *Journal of Petrology* **21**, 498–531.

Neumann, E.-R., Wilson, M., Heeremans, M., Spencer, E. A., Obst, K., Timmerman, M. J. & Kirstein, L. (2004). Carboniferous–Permian rifting and magmatism in southern Scandinavia and northern Germany: a review. In: Wilson, M., Neumann, E.-R., Davies, G. R., Timmerman, M. J., Heeremans, M. & Larsen, B. T. (eds) *Permo-Carboniferous Magmatism and Rifting in Europe. Geological Society, London, Special Publications* **223**, 11–40.

Petersen, J. S. (1978). Structure of the larvikite–lardalite complex, Oslo Region, Norway, and its evolution. *Geologisches Rundschau* **67**, 330–342.

Pfaff, K., Wenzel, T., Schilling, J., Marks, M. A. & Markl, G. (2010). A fast and easy-to-use approach to cation site assignment for eudialyte-group minerals. *Neues Jarhbuch für Mineralogie, Abhandlungen* **187**, 69–81.

Pouchou, J. L. & Pichoir, F. (1984). A new model for quantitative X-ray microanalysisI. Application to the analysis of homogeneous samples. *Recherche Aérospatiale* **3**, 13–38.

Roedder, E. (1984). *Fluid Inclusions. Mineralogical Society of America, Reviews in Mineralogy* **12**, 644 p.

Ryabchikov, I. D. & Kogarko, L. N. (2009). Oxygen fugacity in the apatite-bearing intrusion of the Khibina Complex. *Geochemistry International* **47**, 1157–1169.

Salvi, S. & Williams-Jones, A. E. (1995). Zirconosilicate phase relations in the Strange Lake (Lac Brisson) pluton, Quebec–Labrador, Canada. *American Mineralogist* **80**, 1031–1040.

Schilling, J., Marks, M. A. W., Wenzel, T. & Markl, G. (2009). Reconstruction of magmatic to subsolidus processes in an agpaitic

system using eudialyte textures and composition: a case study from Tamazeght, Morocco. *Canadian Mineralogist* **47**, 351–365.

Sokolova, E. (2006). From structure to chemical composition. I. Structural hierarchy and stereochemistry in titanium disilicate minerals. *Canadian Mineralogist* **44**, 1273–1330.

Sørensen, H. (ed.) (1974). *The Alkaline Rocks*. London: John Wiley, 622 p.

Sørensen, H. (1997). The agpaitic rocks—an overview. *Mineralogical Magazine* **61**, 485–498.

Sørensen, H. (2006). The Ilímaussaq Alkaline Complex, South Greenland—an overiview of 200 years of research and an outlook. *Meddelelser om Grønland, Geoscience* **45**, 1–70.

Strunz, H. & Nickel, E. H. (2001). *Strunz Mineralogical Tables*, 9th edn. Stuttgart: Schweizerbart, 870 p.

Ussing, N. V. (1912). Geology of the country around Julianehaab, Greenland. *Meddelelser om Grønland* **38**, 1–376.

Watson, E. B. & Harrison, M. T. (1983). Zircon saturation revisited: temperature and composition effects in a variety of crustal magma types. *Earth and Planetary Science Letters* **64**, 295–304.

Weibye, P. H. (1850). Neue Mineralien aus Norwegen, beschrieben von P. H. Weibye; analysiert von N. J. Berlin, K. A. Sjögren und J. B. von Borck (Erster Theil). *Annalen der Physik und Chemie* **79**, 299–304.

White, R. W., Powell, R. & Baldwin, J. A. (2008). Calculated phase equilibria involving chemical potentials to investigate the textural evolution of metamorphic rocks. *Journal of Metamorphic Geology* **26**, 181–198.

Zen, E-a. (1966). *Construction of Pressure–Temperature Diagrams for Multicomponent Systems after the Method of Schreinemakers—A Geometric Approach. US Geological Survey Bulletin* **1225**, 56 p.